Fourth-order perturbation theory for the half-filled Hubbard model in infinite dimensions

F. Gebhard[1,a], E. Jeckelmann[2], S. Mahlert[1], S. Nishimoto[1], and R.M. Noack[3]

[1] Fachbereich Physik, Philipps-Universität Marburg, 35032 Marburg, Germany
[2] Institut für Physik, Johannes-Gutenberg Universität Mainz, 55099 Mainz, Germany
[3] Institut für Theoretische Physik III, Universität Stuttgart, 70550 Stuttgart, Germany

Abstract. We calculate the zero-temperature self-energy to fourth-order perturbation theory in the Hubbard interaction U for the half-filled Hubbard model in infinite dimensions. For the Bethe lattice with bare bandwidth W, we compare our perturbative results for the self-energy, the single-particle density of states, and the momentum distribution to those from approximate analytical and numerical studies of the model. Results for the density of states from perturbation theory at $U/W = 0.4$ agree very well with those from the Dynamical Mean-Field Theory treated with the Fixed-Energy Exact Diagonalization and with the Dynamical Density-Matrix Renormalization Group. In contrast, our results reveal the limited resolution of the Numerical Renormalization Group approach in treating the Hubbard bands. The momentum distributions from all approximate studies of the model are very similar in the regime where perturbation theory is applicable, $U/W \leq 0.6$. Iterated Perturbation Theory overestimates the quasiparticle weight above such moderate interaction strengths.

1 Introduction

The Hubbard model serves as a paradigm for strongly correlated electron systems because it combines the two essential aspects of electrons in solids in a simplistic way. It describes spin-1/2 electrons moving on a lattice (bandwidth W) which interact only locally with strength U (Hubbard interaction). Despite its structural simplicity it is thought to encompass a rich phase diagram.

At half band-filling, when there is on average one electron per lattice site, the Hubbard model contains a zero-temperature phase transition from a metal to an insulator, irrespective of any symmetry breaking [1–4]. In the limit of large lattice dimensions [5], the precise nature of this Mott-Hubbard transition is not entirely clear. An exact solution of the problem is not possible, and various approximate treatments have led to two conflicting scenarios; for a review, see references [2,3]. For more recent treatments, see references [6–14].

Discontinuous transition.
The gap jumps to a finite value when the density of states at the Fermi energy becomes zero at some critical interaction strength $U_{c,2}$; the gap is preformed above $U_{c,1} < U_{c,2}$,

and the co-existing insulating state is higher in energy than the metal.

Continuous transition.
The gap opens continuously when the density of states at the Fermi energy becomes zero, $U_{c,1} = U_{c,2} \equiv U_c$.

This situation calls for the development and application of systematic and controlled techniques such as high-order perturbation theory in strong and weak coupling. Recently, some of us [14] investigated the Mott-Hubbard insulator on a Bethe lattice in the limit of large coordination number analytically and numerically. In the present work, after the introduction of some definitions in Section 2, we calculate the one-particle Green function of the metallic state at half band-filling up to and including $\mathcal{O}[(U/W)^4]$ in Section 3; corrections are of the order $(U/W)^6$ due to particle-hole symmetry. Perturbation theory to fourth order is found to converge very well at $U = 0.4W$, but it begins to fail at $U \approx 0.64W$. In Section 4, we compare our perturbative results for the density of states with those of the Dynamical Mean-Field Theory (DMFT), analyzed within two recently developed numerical schemes, the Fixed-Energy Exact Diagonalization (FE-ED) [14] and the Dynamical Density-Matrix Renormalization Group (DDMRG) [15,16]. The DMFT, which becomes exact in the limit of infinite dimensions, requires

a e-mail: florian.gebhard@physik.uni-marburg.de

the self-consistent solution of a single-impurity Anderson model on $n_s \to \infty$ bath sites. We employ the FE-ED for $n_s \leq 15$ and the DDMRG on up to $n_s = 64$ sites. We find very good agreement with our perturbative results for $U = 0.4W$, and can attribute deviations at $U = 0.6W$ to the limited accuracy of fourth-order perturbation theory. Therefore, we conclude that the DDMRG provides a reliable description of the correlated metal at all frequencies. The comparison is less favorable with results from the Numerical Renormalization Group (NRG) [10] and Iterated Perturbation Theory (IPT) which show noticeable deviations for intermediate energies, e.g., in the formation of the Hubbard bands.

In Section 5, we compare our results for the momentum distribution $n(\epsilon)$ and the quasi-particle weight $Z(U)$ with those of the Random Dispersion Approximation (RDA), the NRG and IPT. Within the region of validity of our perturbation expansion, $U \leq 0.6$, the results are almost identical except for the IPT which already overestimates the quasi-particle weight at weak to moderate interaction strengths. Conclusions, Section 6, and two appendices close our presentation.

2 Definitions and basic properties

In this section, we discuss the basic properties of lattice electrons in the limit of infinite dimensions. We define the Hubbard Hamiltonian, the one-particle Green function, and some related one-particle quantities.

2.1 Hamilton operator

We investigate spin-1/2 electrons on a lattice. Their motion is described by

$$\hat{T} = \sum_{\boldsymbol{i},\boldsymbol{j};\sigma} t_{\boldsymbol{i},\boldsymbol{j}} \hat{c}_{\boldsymbol{i},\sigma}^+ \hat{c}_{\boldsymbol{j},\sigma}, \tag{1}$$

where $\hat{c}_{\boldsymbol{i},\sigma}^+$, $\hat{c}_{\boldsymbol{i},\sigma}$ are creation and annihilation operators for electrons with spin $\sigma = \uparrow, \downarrow$ on site $\boldsymbol{i}$. Here $t_{\boldsymbol{i},\boldsymbol{j}}$ are the electron transfer amplitudes between sites $\boldsymbol{i}$ and $\boldsymbol{j}$, and $t_{\boldsymbol{i},\boldsymbol{i}} = 0$. Since we are ultimately interested in the Mott-Hubbard transition we consider a half-filled band where the number of electrons N equals the number of lattice sites L exclusively.

For lattices with translational symmetry, we have $t_{\boldsymbol{i},\boldsymbol{j}} = t(\boldsymbol{i} - \boldsymbol{j})$, and the operator for the kinetic energy is diagonal in momentum space,

$$\hat{T} = \sum_{\boldsymbol{k};\sigma} \epsilon(\boldsymbol{k}) \hat{c}_{\boldsymbol{k},\sigma}^+ \hat{c}_{\boldsymbol{k},\sigma},$$

$$\epsilon(\boldsymbol{k}) = \frac{1}{L} \sum_{\boldsymbol{i},\boldsymbol{j}} t(\boldsymbol{i} - \boldsymbol{j}) e^{-\mathrm{i}(\boldsymbol{i}-\boldsymbol{j})\boldsymbol{k}}. \tag{2}$$

The density of states for non-interacting electrons is then given by

$$\rho(\epsilon) = \frac{1}{L} \sum_{\boldsymbol{k}} \delta(\epsilon - \epsilon(\boldsymbol{k})). \tag{3}$$

The mth moment of the density of states is defined by

$$\overline{\epsilon^m} = \int_{-\infty}^{\infty} \mathrm{d}\epsilon \, \epsilon^m \rho(\epsilon), \tag{4}$$

and $\overline{\epsilon} = t(\boldsymbol{0}) = 0$.

In the limit of high lattice dimensions and for translationally invariant systems, the Hubbard model is characterized by $\rho(\epsilon)$ alone, i.e., higher-order correlation functions in momentum space factorize, e.g. [17],

$$\rho_{\boldsymbol{q}_1,\boldsymbol{q}_2}(\epsilon_1, \epsilon_2) \equiv \frac{1}{L} \sum_{\boldsymbol{k}} \delta(\epsilon_1 - \epsilon(\boldsymbol{k} + \boldsymbol{q}_1)) \delta(\epsilon_2 - \epsilon(\boldsymbol{k} + \boldsymbol{q}_2))$$

$$= \rho(\epsilon_1)[\delta_{\boldsymbol{q}_1,\boldsymbol{q}_2} \delta(\epsilon_1 - \epsilon_2) + (1 - \delta_{\boldsymbol{q}_1,\boldsymbol{q}_2})\rho(\epsilon_2)]. \tag{5}$$

This observation is the basis for the Random Dispersion Approximation (RDA) which becomes exact in infinite dimensions for paramagnetic systems where nesting is ignored [2,6]; see Section 5.

In the following, we assume a symmetric bare density of states, $\rho(-\epsilon) = \rho(\epsilon)$, of width W. For our explicit calculations we shall later use the semi-circular density of states

$$\rho_0(\omega) = \frac{2}{\pi W} \sqrt{4 - \left(\frac{4\omega}{W}\right)^2}, \quad (|\omega| \leq W/2), \tag{6}$$

where $W \equiv 4t$ is the bandwidth. In the following, we shall set $t \equiv 1$ as our energy unit if not otherwise explicitly stated. This density of states is realized for non-interacting tight-binding electrons on a Bethe lattice of connectivity $Z \to \infty$ [18], i.e., each site is connected to Z neighbors without generating closed loops, and the electron transfer is restricted to nearest-neighbors, $t_{\boldsymbol{i},\boldsymbol{j}} = -1/\sqrt{Z}$ for $\boldsymbol{i}$ and $\boldsymbol{j}$ being nearest neighbors and zero otherwise. The limit $Z \to \infty$ is implicitly understood henceforth.

The electrons are assumed to interact only locally, and the Hubbard interaction reads

$$\hat{D} = \sum_{\boldsymbol{i}} \left(\hat{n}_{\boldsymbol{i},\uparrow} - \frac{1}{2}\right) \left(\hat{n}_{\boldsymbol{i},\downarrow} - \frac{1}{2}\right), \tag{7}$$

where $\hat{n}_{\boldsymbol{i},\sigma} = \hat{c}_{\boldsymbol{i},\sigma}^+ \hat{c}_{\boldsymbol{i},\sigma}$ is the local density operator at site $\boldsymbol{i}$ for spin σ. This leads to the Hubbard model [19],

$$\hat{H} = \hat{T} + U\hat{D}. \tag{8}$$

The Hamiltonian exhibits explicit particle-hole symmetry, i.e., $\hat{H}$ is invariant under the transformation

$$\mathrm{PH}: \qquad \hat{c}_{\boldsymbol{i},\sigma}^+ \mapsto (-1)^{\boldsymbol{i}} \hat{c}_{\boldsymbol{i},\sigma}; \quad \hat{c}_{\boldsymbol{i},\sigma} \mapsto (-1)^{\boldsymbol{i}} \hat{c}_{\boldsymbol{i},\sigma}^+. \tag{9}$$

For the Bethe lattice $(-1)^{\boldsymbol{i}} = +1$ for the A sites which are surrounded by B sites only (and vice versa), for which $(-1)^{\boldsymbol{i}} = -1$. A chemical potential $\mu = 0$ then guarantees a half-filled band for all temperatures [2].

2.2 Green functions and self-energy

The time-dependent single-particle Green function at zero temperature is given by [20]

$$G_\sigma(\boldsymbol{i}, \boldsymbol{j}; t) = -\mathrm{i}\langle \hat{\mathcal{T}}[\hat{c}_{\boldsymbol{i},\sigma}(t)\hat{c}^+_{\boldsymbol{j},\sigma}]\rangle. \tag{10}$$

Here $\hat{\mathcal{T}}$ is the time-ordering operator, $\langle \ldots \rangle$ implies the expectation value in the ground state with energy E_0, and ($\hbar \equiv 1$)

$$\hat{c}_{\boldsymbol{i},\sigma}(t) = \exp(\mathrm{i}\hat{H}t)\hat{c}_{\boldsymbol{i},\sigma}\exp(-\mathrm{i}\hat{H}t) \tag{11}$$

is the annihilation operator in the Heisenberg picture. For translationally invariant systems, the Fourier transform of the Green function is given by

$$G_\sigma(\boldsymbol{k}, \omega) = \int_{-\infty}^{\infty} \mathrm{d}t\, e^{\mathrm{i}\omega t}\frac{1}{L}\sum_{\boldsymbol{i},\boldsymbol{j}} e^{-\mathrm{i}\boldsymbol{k}(\boldsymbol{i}-\boldsymbol{j})} G_\sigma(\boldsymbol{i}, \boldsymbol{j}; t). \tag{12}$$

The Green function in momentum space can be expressed in terms of the self-energy $\Sigma_\sigma(\boldsymbol{k}, \omega)$ [20] ($\eta = 0^+$),

$$G_\sigma(\boldsymbol{k}, \omega) = \frac{1}{\omega - \epsilon(\boldsymbol{k}) - \Sigma_\sigma(\boldsymbol{k}, \omega) + \mathrm{i}\eta\mathrm{sgn}(\omega)}. \tag{13}$$

In the limit of infinite dimensions, the self-energy is independent of momentum [5], $\Sigma_\sigma(\boldsymbol{k}, \omega) = \Sigma_\sigma(\omega)$. As we shall further discuss in Section 3, the self-energy can be calculated in a power series in U. As shown by Luttinger [21], it has the following properties at small frequency,

$$\Re\Sigma_\sigma(\omega) = \left(1 - \frac{1}{Z}\right)\omega; \quad 0 \le \omega < \omega_c, \tag{14}$$

$$\Im\Sigma_\sigma(\omega) = -\gamma\omega^2; \quad 0 \le \omega < \omega_c. \tag{15}$$

Here $0 < Z \le 1$, $\gamma \ge 0$, and a low-energy cut-off $\omega_c \ll W$ characterize a Fermi liquid.

The local Green function $G_\sigma(\omega)$ is the momentum-space average of $G_\sigma(\boldsymbol{k}, \omega)$,

$$\begin{aligned} G_\sigma(\omega) &= \frac{1}{L}\sum_{\boldsymbol{i}}\int_{-\infty}^{\infty} \mathrm{d}t\, e^{\mathrm{i}\omega t} G_\sigma(\boldsymbol{i}, \boldsymbol{i}; t) \\ &= \frac{1}{L}\sum_{\boldsymbol{k}} G_\sigma(\boldsymbol{k}, \omega) \\ &= \int_{-\infty}^{\infty} \mathrm{d}\epsilon\, \rho(\epsilon)\frac{1}{\omega - \epsilon - \Sigma_\sigma(\omega) + \mathrm{i}\eta\mathrm{sgn}(\omega)}. \end{aligned} \tag{16}$$

Due to particle-hole symmetry, the local Green function obeys $G_\sigma(t) = -G_\sigma(-t)$ so that $G_\sigma(\omega) = -G_\sigma(-\omega)$, and thus $\Sigma_\sigma(\omega) = -\Sigma_\sigma(-\omega)$.

Because the self-energy only depends on frequency, the local Green function can be easily recovered from the self-energy. As seen from (16),

$$G_\sigma(\omega) = G_\sigma^0(\omega - \Sigma_\sigma(\omega)). \tag{17}$$

This relation is particularly simple for the semi-circular density of states (6) where

$$G_\sigma^0(z) = \frac{z}{2}\left[1 - \sqrt{1 - \frac{4}{z^2}}\right], \tag{18}$$

with $z = \omega + \mathrm{i}\eta\mathrm{sgn}(\omega)$. For the Bethe lattice it then follows that

$$\omega - \Sigma_\sigma(\omega) = G_\sigma(\omega) + G_\sigma^{-1}(\omega). \tag{19}$$

With the help of a full set of eigenstates $|\Psi_n\rangle$, we can write the local Green function in the Lehmann representation [20]

$$G_\sigma(\omega) = \int_{-\infty}^{\infty} \mathrm{d}\omega'\frac{D_\sigma(\omega')}{\omega - \omega' + \mathrm{i}\eta\mathrm{sgn}(\omega')}$$

$$D_\sigma(\omega \ge 0) = \sum_n \frac{1}{L}\sum_{\boldsymbol{i}} |\langle\Psi_0|\hat{c}_{\boldsymbol{i},\sigma}|\Psi_n\rangle|^2\, \delta(\omega + E_0 - E_n). \tag{20}$$

Consequently, the density of states is obtained from the imaginary part of the local Green function (17) via

$$D_\sigma(\omega) = -\frac{1}{\pi}\mathrm{sgn}(\omega)\Im G_\sigma(\omega) = D_\sigma(-\omega). \tag{21}$$

The latter equality holds due to particle-hole symmetry. For a Fermi liquid, (14) and (15) in (17) lead to

$$D_\sigma(0) = \rho(0), \tag{22}$$

i.e., the density of states at $\omega = 0$ is pinned to its value at $U = 0$ [22].

The moments M_n of the density of states are defined as

$$M_n = 2\int_0^{\infty} \mathrm{d}\omega\, \omega^n D_\sigma(\omega). \tag{23}$$

In particular, from (20), (21), and the definition of the Green function (10) one can show that [20]

$$M_1 = -\frac{1}{L}\left(E_0 + U\frac{\partial E_0}{\partial U}\right). \tag{24}$$

We will later employ this useful sum rule for calculating the ground-state energy.

The one-particle spectral function $A_\sigma(\epsilon; \omega)$ is symmetric in ω. It is defined by ($\omega \ge 0$)

$$\begin{aligned} A_\sigma(\epsilon; \omega) &= -\frac{1}{\pi}\Im\left(\frac{1}{\omega - \epsilon - \Sigma_\sigma(\omega) + \mathrm{i}\eta}\right) \\ &= -\frac{1}{\pi}\frac{(\Im\Sigma_\sigma(\omega) - \eta)}{(\omega - \epsilon - \Re\Sigma_\sigma(\omega))^2 + (\Im\Sigma_\sigma(\omega) - \eta)^2}. \end{aligned} \tag{25}$$

Note that

$$D_\sigma(\omega) = \int_{-\infty}^{\infty} \mathrm{d}\epsilon\, \rho(\epsilon) A_\sigma(\epsilon; \omega). \tag{26}$$

As follows from the Lehmann representation [20], the spectral function is positive semi-definite, $A_\sigma(\epsilon; \omega) \ge 0$, so that

$$\Im\Sigma_\sigma(\omega \ge 0) \le 0. \tag{27}$$

The spectral function contains a quasi-particle contribution of weight $Z(U)$ near the Fermi energy and an incoherent background contribution,

$$A_\sigma(\epsilon; \omega \to 0) = Z(U)\delta(\omega - Z(U)\epsilon) + A_\sigma^{\mathrm{inc}}(\epsilon; \omega \to 0). \tag{28}$$

The momentum distribution

$$n_\sigma(\epsilon) = \int_{-\infty}^{0} \mathrm{d}\omega\, A_\sigma(\epsilon; \omega) \qquad (29)$$

depends on momentum only implicitly via $\epsilon \equiv \epsilon(\boldsymbol{k})$. In the metallic phase, $n_\sigma(\epsilon)$ displays a jump discontinuity at the Fermi energy,

$$n_\sigma(\epsilon = 0^-) - n_\sigma(\epsilon = 0^+) = Z(U), \qquad (30)$$

as follows directly from (14), (15), (29) and the fact that the self-energy does not depend on momentum. In the vicinity of $\epsilon = 0$, the momentum distribution takes the form ($E \equiv Z(U)\epsilon/\omega_c$)

$$n_\sigma(E \ll 1) = \frac{1 - Z(U)}{2} + \frac{2\gamma\omega_c Z(U)^2}{\pi} E \ln E + \mathcal{O}(E). \qquad (31)$$

This is shown in Appendix A.

3 Diagrammatic perturbation theory

In this section we derive and calculate the diagrams to second and fourth order perturbation theory in U.

3.1 Second order

The particle-hole transformation (9) can be restricted to one spin species only. The Hamiltonian then maps onto itself apart from a change in the sign of U. Therefore, the Green function obeys

$$G_\sigma(\omega; U) = G_\sigma(\omega; -U), \qquad (32)$$

and, correspondingly, the self-energy fulfills

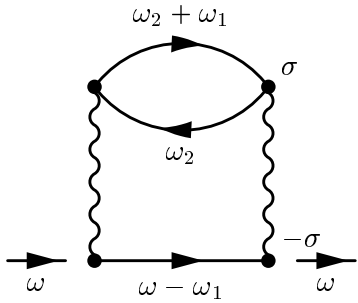$$\Sigma_\sigma(\omega; U) = \Sigma_\sigma(\omega; -U). \qquad (33)$$

Consequently, there are no odd orders in the perturbation expansion of the self-energy in U.

Particle-hole symmetry also guarantees that there are no (renormalized) Hartree bubbles. A chemical potential $\mu = 0$ results in [2]

$$\frac{1}{L}\sum_{\boldsymbol{i}} \langle \hat{n}_{\boldsymbol{i}} \rangle = \frac{1}{L}\sum_{\boldsymbol{i}} \langle \hat{n}_{\boldsymbol{i}} \rangle_0 = \frac{1}{2}, \qquad (34)$$

i.e., the bare Hartree diagrams are exactly canceled by definition of the Hubbard interaction in (7), and, moreover, the renormalized Hartree diagram vanishes to all orders in perturbation theory. Lastly, there are no Fock contributions because the Hubbard interaction acts between different spin species only.

With these simplifications, only one diagram remains in second-order perturbation theory,

$$\Sigma_{-\sigma}^{(2)}(\omega) = \qquad\qquad\qquad\qquad . \qquad (35)$$

Three independent Green function lines connect the two lattice points. Thus, in the limit of infinite dimensions, they can be identified with each other [5], and each line thus represents a local bare Green function $G_\sigma^0(\omega_i) = G_{-\sigma}^0(\omega_i)$ due to spin symmetry. Note, however, that energy conservation must still be obeyed at each vertex. Following the Feynman rules, the second-order diagram gives the contribution [22,23]

$$\Sigma_{-\sigma}^{(2)}(\omega) = (-1)(\mathrm{i})^2 U^2 \int_{-\infty}^{\infty} \frac{\mathrm{d}\omega_1}{2\pi\mathrm{i}} G_{-\sigma}^0(\omega - \omega_1) \Pi_\sigma^0(\omega_1) \quad (36)$$

with the bare polarization bubble

$$\Pi_\sigma^0(\omega) = -\int_{-\infty}^{\infty} \frac{\mathrm{d}\omega_2}{2\pi\mathrm{i}} G_\sigma^0(\omega_2) G_\sigma^0(\omega_2 + \omega) = \Pi_\sigma^0(-\omega). \qquad (37)$$

With the help of the spectral representation (16) of the local bare Green function

$$G_\sigma^0(\omega) = \int_0^{W/2} \mathrm{d}\epsilon\, \rho(\epsilon) \left(\frac{1}{\omega - \epsilon + \mathrm{i}\eta} + \frac{1}{\omega + \epsilon - \mathrm{i}\eta} \right), \quad (38)$$

a contour integration results in

$$\Pi_\sigma^0(\omega) = -\int_0^{W/2} \mathrm{d}\epsilon_1 \int_0^{W/2} \mathrm{d}\epsilon_2\, \rho(\epsilon_1)\rho(\epsilon_2)$$
$$\times \left(\frac{1}{\omega - \epsilon_1 - \epsilon_2 + \mathrm{i}\eta} - \frac{1}{\omega + \epsilon_1 + \epsilon_2 - \mathrm{i}\eta} \right). \qquad (39)$$

Taking the imaginary part gives

$$\frac{1}{\pi} \Im \Pi_\sigma^0(\omega \geq 0) = \int_0^\omega \mathrm{d}\epsilon\, \rho(\epsilon)\rho(\omega - \epsilon). \qquad (40)$$

This representation explicitly shows that the imaginary part of the bare polarization bubble vanishes for $|\omega| \geq W$. This is a consequence of the fact that the bare polarization bubble is made up of two bare Green function lines.

Using the spectral representation of the bare polarization bubble (39) and of the local Green function (38) in (36), the contour integration over ω_1 can easily be performed. Taking the imaginary part leads to

$$\Im \Sigma_{-\sigma}^{(2)}(\omega \geq 0) = -U^2 \int_0^\omega \mathrm{d}\epsilon\, \rho(\epsilon) \Im \Pi_\sigma^0(\omega - \epsilon). \qquad (41)$$
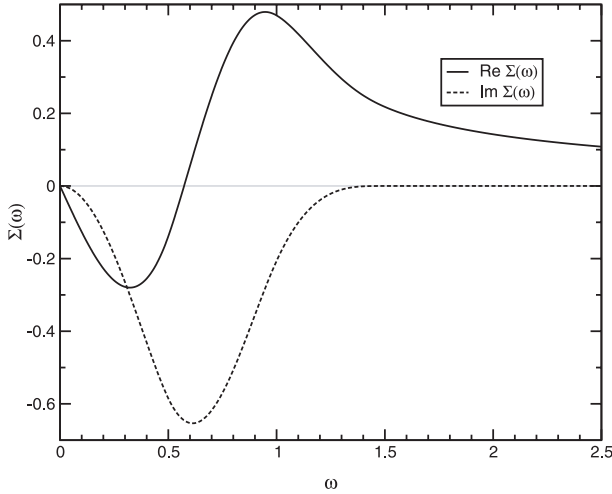
Fig. 1. Real and imaginary part of the second-order self-energy; units $W = 4t \equiv 1$.

The imaginary part of the second-order self-energy vanishes for $|\omega| \geq 3W/2$. The Hilbert transformation provides the real part as

$$\Re\Sigma_{-\sigma}^{(2)}(\omega) = \frac{1}{\pi}\mathcal{P}\int_0^{3W/2}\mathrm{d}\zeta\,\Im\Sigma_{-\sigma}^{(2)}(\zeta)\left(\frac{1}{\zeta-\omega}-\frac{1}{\zeta+\omega}\right).\tag{42}$$

For practical calculations it is advisable to split the integration routines into intervals $[(r-1)W/2, rW/2]$ ($r = 1, 2, 3$) in order to speed up the integrations and to minimize numerical errors.

For the density of states of the Bethe lattice (6), the result for the real and imaginary parts of the second-order self-energy are shown in Figure 1, apart from the prefactor U^2. As seen from the figure, the self-energy reproduces the Fermi-liquid relations (14) and (15) for small frequencies. Explicitly, we find from our numerical integrations

$$Z(U)^{-1} = 1 + 1.307[1]\left(\frac{U}{W}\right)^2 + \mathcal{O}(U^4)\tag{43}$$

and

$$\gamma(U) = 3.242[1]\left(\frac{U}{W}\right)^2 + \mathcal{O}(U^4),\tag{44}$$

where the number in brackets denotes the uncertainty in the last digit.

3.2 Fourth order

The twelve topologically different diagrams to fourth order can be grouped into four sets; see below. They were used earlier by Yamada and Yosida [24] in their study of the symmetric Anderson impurity model, and by Freericks and Jarrell [25] in their finite-temperature perturbation study of the Hubbard model. With the help of particle-hole symmetry it is not difficult to show that the diagrams
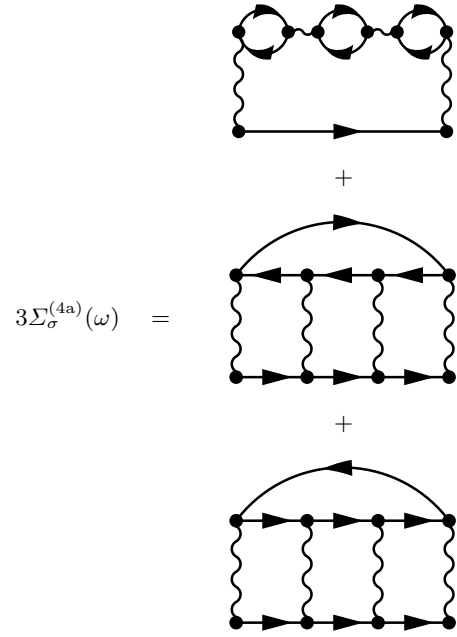

Fig. 2. Set A of three equivalent diagrams to the proper self-energy in fourth-order perturbation theory.

of each set give the same contribution [25]. We also find

$$\Sigma_\sigma^{(4)}(\omega) = 3\left(\Sigma_\sigma^{(4a)}(\omega) + \Sigma_\sigma^{(4b)}(\omega) + \Sigma_\sigma^{(4c)}(\omega) + \Sigma_\sigma^{(4d)}(\omega)\right).\tag{45}$$

We discuss the diagrams of the four sets and their contributions to the self-energy in the following.

3.2.1 Ring diagram

The ring diagram in Figure 2 and the particle-hole/particle-particle ladders give identical contributions at half band-filling. This is most easily seen when the Feynman rules are applied in the time domain, and particle-hole symmetry, $G_\sigma(t) = -G_\sigma(-t)$, is used appropriately. For the ring diagram the Feynman rules result in

$$\tag{46}$$

In order to evaluate this diagram, we define

$$P(\omega) = \left[\Pi_\sigma^0(\omega)\right]^3.\tag{47}$$

Analogously to the second-order calculation, we then find

$$\Im\Sigma_\sigma^{(4a)}(\omega \geq 0) = -U^4\int_0^\omega \mathrm{d}\epsilon\,\rho(\epsilon)\Im P(\omega-\epsilon)\tag{48}$$
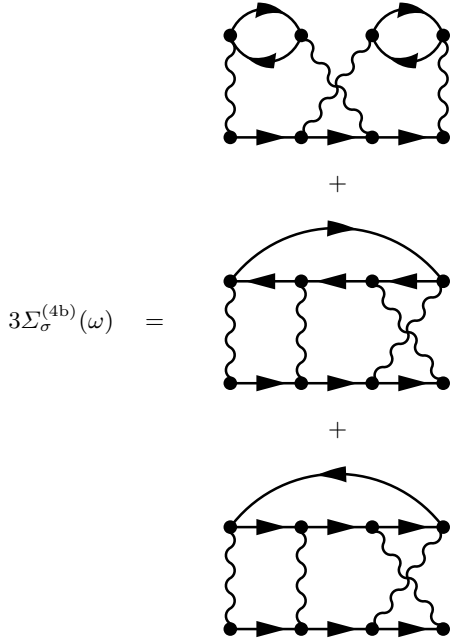
Fig. 3. Set B of three equivalent diagrams to the proper self-energy in fourth-order perturbation theory.

with

$$\Im P(\omega) = \Im \Pi^0_\sigma(\omega) \left[3(\Re \Pi^0_\sigma(\omega))^2 - (\Im \Pi^0_\sigma(\omega))^2 \right]. \quad (49)$$

The real part $\Re \Pi^0_\sigma(\omega)$ is obtained via Hilbert transformation of $\Im \Pi^0_\sigma(\omega)$; see Appendix B.

3.2.2 Second-order diagram with second-order vertex correction

The second-order diagram with second-order vertex correction in Figure 3 and the particle-hole/particle-particle ladders with crossed interaction lines give identical contributions at half band-filling. For the second-order diagram with second-order vertex correction, the Feynman rules result in

$$(50)$$

Explicitly,

$$\Sigma^{(4b)}_\sigma(\omega) = U^4 \int_{-\infty}^{\infty} \frac{d\omega_1}{2\pi i} \int_{-\infty}^{\infty} \frac{d\omega_3}{2\pi i} G^0_\sigma(\omega - \omega_1) \Pi^0_\sigma(\omega_1)$$
$$\times G^0_\sigma(\omega - \omega_1 - \omega_3) G^0_\sigma(\omega - \omega_3) \Pi^0_\sigma(\omega_3). \quad (51)$$

The contour integration over ω_3 can be performed using the spectral representation of the bare polarization bubble (39) and of the local Green function (38) in (51). The remaining contour integral over ω_1 then results in 24 terms, four of which are zero. When we restrict ourselves to $\omega > 0$ and focus on the imaginary part, another four terms vanish. A change in integration variables shows that six terms come in pairs. Thus, only ten different terms need to be evaluated [26]. The calculation of the imaginary part reduces the seven-fold integrations over the bare density of states to six-fold integrations. Fortunately, these integrations can be grouped so that the final result can be expressed in terms of help functions which can be tabulated and used in the remaining at most two-fold integrations over finite energy intervals. These help functions are listed in Appendix B.

The ten remaining terms lead to 20 integrals which can be expressed using the bare density of states and the help functions. Appropriate changes in the energy integration variables allow us to regroup them into six terms,

$$\Im \Sigma^{(4b)}_\sigma(\omega \geq 0) = \pi U^4 \sum_{i=1}^{6} I_i \quad (52)$$

with

$$I_1 = - \int_0^W da\, h(a) \int_0^W db\, h(b)$$
$$\times \widetilde{\rho}(\omega - a - b) l(b - \omega) l(a - \omega), \quad (53)$$

$$I_2 = -2 \int_0^W db\, h(b) \int_0^{W/2} d\epsilon_1 \rho(\epsilon_1) h(\omega - \epsilon_1)$$
$$\times \left[f(b - \omega) f(b - \epsilon_1) + f(b + \omega) f(b + \epsilon_1) \right], \quad (54)$$

$$I_3 = 2 \int_0^W da\, h(a) \widetilde{\rho}(\omega - a) \int_0^{W/2} d\epsilon_1 \rho(\epsilon_1) f(\epsilon_1 + a)$$
$$\times \left[H(\epsilon_1 + a - \omega) + H(\omega + \epsilon_1) \right], \quad (55)$$

$$I_4 = \pi^2 \int_0^W da\, h(a) \int_0^W db\, h(b) \widetilde{\rho}(\omega - a) \widetilde{\rho}(\omega - b)$$
$$\times \left[\widetilde{\rho}(\omega - a - b) - \widetilde{\rho}(a + b - \omega) \right], \quad (56)$$

$$I_5 = 2 \int_0^{W/2} d\epsilon_1 \rho(\epsilon_1) \int_0^{W/2} d\epsilon_2 \rho(\epsilon_2) h(\omega - \epsilon_1)$$
$$\times f(\epsilon_1 + \epsilon_2 - \omega) \times \left[H(\epsilon_1 + \epsilon_2) + H(\epsilon_2 - \omega) \right], \quad (57)$$

$$I_6 = \int_0^{W/2} d\epsilon_1 \rho(\epsilon_1) \int_0^{W/2} d\epsilon_2 \rho(\epsilon_2) \widetilde{\rho}(\omega - \epsilon_1 - \epsilon_2)$$
$$\times \Big[2H(\epsilon_2 - \omega) H(\epsilon_1 + \epsilon_2) + H(\omega - \epsilon_2) H(\epsilon_1 + \epsilon_2)$$
$$+ H(\epsilon_1 - \omega) H(\epsilon_2 - \omega) \Big], \quad (58)$$

where $\widetilde{\rho}(x) = \rho(x) \Theta(x)$. For practical calculations, it is advisable to split the integration routines into intervals $[(r-1)W/2, rW/2]$ $(r = 1, \ldots, 5)$ in order to speed up the integrations and to minimize numerical errors. We have checked our results against a numerical integration in the
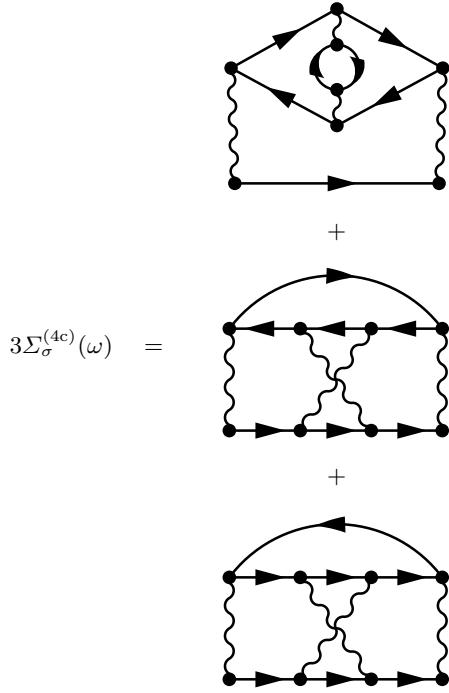
Fig. 4. Set C of three equivalent diagrams to the proper self-energy in fourth-order perturbation theory.

time domain which is easier to implement but much less accurate for the same computational effort.

3.2.3 Second-order diagram with vertex correction in the polarization bubble

The second-order diagram with vertex correction in the polarization bubble in Figure 4 and the particle-hole/particle-particle ladders with crossed interaction lines give identical contributions at half band-filling. For the second-order diagram with second-order vertex corrections in the polarization bubble, the Feynman rules result in

$$\Sigma_\sigma^{(4c)}(\omega) = \qquad (59)$$

Obviously, we may split off the renormalized polarization bubble. Analogously to the second-order calculation, we immediately arrive at

$$\Im\Sigma_\sigma^{(4c)}(\omega \geq 0) = -U^4 \int_0^\omega \mathrm{d}\epsilon \rho(\epsilon) \Im\Pi_V(\omega - \epsilon) \qquad (60)$$

with

$$\Pi_V(x) = -\int_{-\infty}^\infty \frac{\mathrm{d}\omega_2}{2\pi\mathrm{i}} \int_{-\infty}^\infty \frac{\mathrm{d}\omega_4}{2\pi\mathrm{i}} G_\sigma^0(\omega_4) G_\sigma^0(\omega_4 - x)$$
$$\times G_\sigma^0(\omega_4 - \omega_2) G_\sigma^0(\omega_4 - x - \omega_2) \Pi_\sigma^0(\omega_2), \quad (61)$$

which is symmetric in x.

Using the spectral representation of the bare polarization bubble (39) and of the local Green function (38) in (61), the contour integration over ω_2 results in six non-vanishing terms. The remaining contour integral over ω_4 then gives 24 terms of which seven are zero, and four come in pairs. Of the remaining 13 terms, five do not provide a finite imaginary part for $x \geq 0$. A re-grouping of integration variables shows that only five different terms remain for $x \geq 0$,

$$\Im\Pi_V(x) = 2\Im \int_0^\infty \mathrm{d}\epsilon_1 \rho(\epsilon_1) \ldots \int_0^\infty \mathrm{d}\epsilon_6 \rho(\epsilon_6)$$

$$\times \left\{ \frac{1}{x + \epsilon_1 + \epsilon_3 + \epsilon_4 + \epsilon_6} \frac{1}{\epsilon_1 + \epsilon_3 + \epsilon_4 + \epsilon_5} \right.$$

$$\times \frac{1}{x + \epsilon_1 - \epsilon_2 - \mathrm{i}\eta_1 \mathrm{sgn}(\epsilon_1 - \epsilon_2)}$$

$$+ \frac{1}{x - \epsilon_2 - \epsilon_3 - \epsilon_4 - \epsilon_5 + \mathrm{i}\eta_3} \frac{1}{\epsilon_2 + \epsilon_3 + \epsilon_4 + \epsilon_6}$$

$$\times \frac{1}{x + \epsilon_1 - \epsilon_2 - \mathrm{i}\eta_1 \mathrm{sgn}(\epsilon_1 - \epsilon_2)}$$

$$+ 2\frac{1}{x - \epsilon_1 - \epsilon_2 + \mathrm{i}\eta_1} \frac{1}{x - \epsilon_2 - \epsilon_3 - \epsilon_4 - \epsilon_5 + \mathrm{i}\eta_5}$$

$$\times \frac{1}{\epsilon_2 + \epsilon_3 + \epsilon_4 + \epsilon_6}$$

$$+ 2\frac{1}{x - \epsilon_1 - \epsilon_2 + \mathrm{i}\eta_1} \frac{1}{x + \epsilon_5 + \epsilon_6 - \mathrm{i}\eta_2}$$

$$\times \frac{1}{\epsilon_2 + \epsilon_3 + \epsilon_4 + \epsilon_6}$$

$$+ \frac{1}{x - \epsilon_1 - \epsilon_2 + \mathrm{i}\eta_1} \frac{1}{x - \epsilon_5 - \epsilon_6 + \mathrm{i}\eta_2}$$

$$\left. \times \frac{1}{x - \epsilon_2 - \epsilon_3 - \epsilon_4 - \epsilon_5 + \mathrm{i}\eta_3} \right\}. \quad (62)$$

Taking the imaginary part simplifies this expression. First, the terms with the common factor $\mathrm{sgn}(\epsilon_1 - \epsilon_2)\delta(x + \epsilon_1 - \epsilon_2)$ cancel each other. Second, we are left with five-fold integrations over finite intervals. Third, these expressions can be simplified further using the help functions of Appendix B. We find

$$\Im\Pi_V(x \geq 0) = -2\pi \sum_{i=1}^7 J_i \qquad (63)$$

with

$$J_1 = \int_0^{W/2} d\epsilon_2 \int_0^W dy$$

$$\times h(y)\rho(\epsilon_2)\widetilde{\rho}(x - \epsilon_2 - y)f(x - \epsilon_2)f(\epsilon_2 + y), \quad (64)$$

$$J_2 = -2 \int_0^{W/2} d\epsilon_2 \int_0^W dy$$

$$\times h(y)\rho(\epsilon_2)\widetilde{\rho}(x - \epsilon_2)f(\epsilon_2 + y - x)f(\epsilon_2 + y), \quad (65)$$

$$J_3 = -2 \int_0^{W/2} d\epsilon_2 \int_0^W dy$$

$$\times h(y)\rho(\epsilon_2)\widetilde{\rho}(x - \epsilon_2 - y)f(\epsilon_2 - x)f(\epsilon_2 + y), \quad (66)$$

$$J_4 = 2 \int_0^{W/2} d\epsilon_2 \int_0^{W/2} d\epsilon_6$$

$$\times \rho(\epsilon_2)\rho(\epsilon_6)\widetilde{\rho}(x - \epsilon_2)f(x + \epsilon_6)H(\epsilon_2 + \epsilon_6), \quad (67)$$

$$J_5 = 2 \int_0^{W/2} d\epsilon_2 \int_0^{W/2} d\epsilon_5$$

$$\times \rho(\epsilon_2)\rho(\epsilon_5)\widetilde{\rho}(x - \epsilon_2)f(\epsilon_5 - x)H(\epsilon_2 + \epsilon_5 - x), (68)$$

$$J_6 = \int_0^{W/2} d\epsilon_2 \int_0^{W/2} d\epsilon_5$$

$$\times \rho(\epsilon_2)\rho(\epsilon_5)f(\epsilon_2 - x)f(\epsilon_5 - x)h(x - \epsilon_2 - \epsilon_5), (69)$$

$$J_7 = -\pi^2 \int_0^{W/2} d\epsilon_2 \int_0^{W/2} d\epsilon_5$$

$$\times \rho(\epsilon_2)\rho(\epsilon_5)\widetilde{\rho}(x - \epsilon_2)\widetilde{\rho}(x - \epsilon_5)h(x - \epsilon_2 - \epsilon_5), (70)$$

where $\widetilde{\rho}(x) = \rho(x)\Theta(x)$. For practical calculations it is advisable to split the integration routines into intervals $[(r-1)W/2, rW/2]$ $(r = 1, \ldots, 4)$ in order to speed up the integrations and to minimize numerical errors. We have checked our results against a numerical integration in the time domain.

3.2.4 Second-order diagram with second-order self-energy insertion

The second-order diagrams with self-energy insertion in Figure 5 give identical contributions in the paramagnet at half band-filling. These diagrams are not skeleton diagrams so that momentum conservation cannot be ignored at the inner vertices.
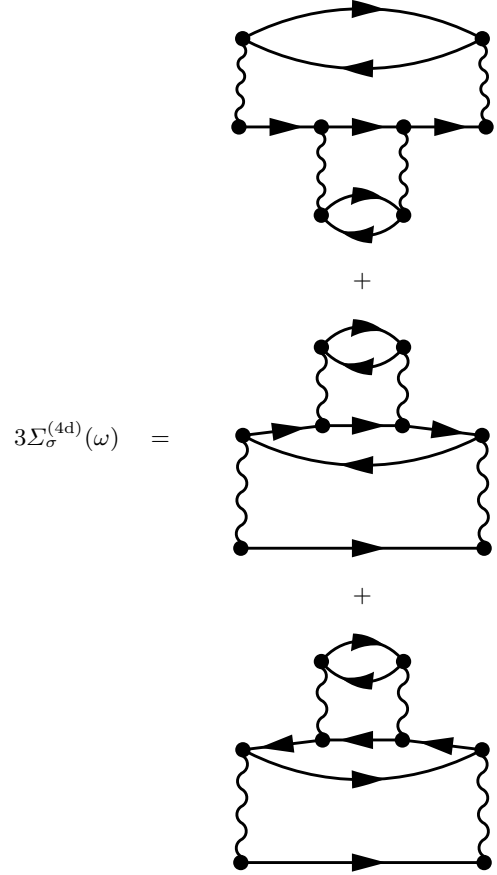

Fig. 5. Set D of three equivalent diagrams to the proper self-energy in fourth-order perturbation theory.

For the second-order diagram with self-energy insertion, the Feynman rules result in

$$(71)$$

Obviously, we may use the results for the bare polarization bubble and the second-order self-energy to simplify the expression to the form

$$\Sigma_\sigma^{(4d)}(\omega) = U^2 \int_{-\infty}^\infty \frac{d\omega_1}{2\pi i} \Pi_\sigma^0(\omega_1) \Sigma_\sigma^{(2)}(\omega - \omega_1)$$

$$\times \frac{1}{L} \sum_{\boldsymbol{k}} [G_\sigma^0(\epsilon(\boldsymbol{k}); \omega - \omega_1)]^2. \quad (72)$$

Fig. 6. Imaginary part of the fourth-order self-energy diagrams; units $W = 4t \equiv 1$.

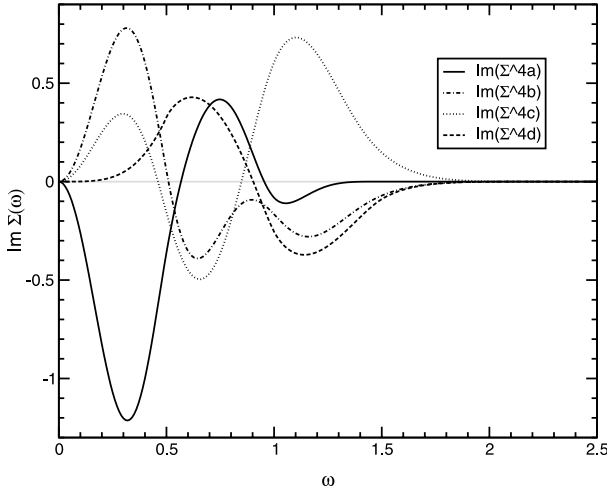**Fig. 7.** Real and imaginary part of the fourth-order self-energy; units $W = 4t \equiv 1$.

We must evaluate

$$\frac{1}{L} \sum_{\boldsymbol{k}} [G_\sigma^0(\epsilon(\boldsymbol{k}); x)]^2 = A_+(x) + A_-(x), \qquad (73)$$

with

$$A_\pm(x) = \int_0^{W/2} \mathrm{d}y \rho(y) \frac{1}{x \mp y \pm \mathrm{i}\eta_3} \frac{1}{x \mp y \pm \mathrm{i}\eta_4}. \qquad (74)$$

We may set $\eta_3 = \eta_4$ later so that $A_\pm(x)$ may be expressed in terms of $\rho(0)$ and the derivative of the bare density of states, $d(x) = (\mathrm{d}\rho(x))/(\mathrm{d}x)$.

The spectral representations of $A_\pm(x)$ in (74), $\Pi_\sigma^0(\omega)$ in (128), and $\Sigma_\sigma^{(2)}(\omega)$ in (131) allow us to perform the contour integral over ω_1 in (72) with the result

$$\Im \Sigma_\sigma^{(4\mathrm{d})}(\omega) = \pi U^4 \int_0^{W/2} \mathrm{d}x\, d(x) h(\omega - x)[S(x) - S(-x)]$$
$$+ \pi U^4 \int_0^{3W/2} \mathrm{d}b\, s(b) h(\omega - b) l'(b), \quad (75)$$

where $l'(b)$ denotes the derivative of the help function $l(b)$, see (124). Again, it is advisable to split the integration routines into intervals $[(r-1)W/2, rW/2]$ $(r = 1, \ldots, 5)$ in order to speed up the integrations and to minimize numerical errors.

The result for the real and imaginary parts of the fourth-order diagrams are shown in Figure 6, apart from the prefactor U^4. As seen from the figure, the diagrams are equally important. At half band-filling there is generally no reason to include only special diagram classes, as done, e.g., in the RPA or in the ladder approximation. In particular, for small ω the contribution of the fourth-order ring diagram is to a large extent canceled by the two diagrams with vertex corrections.

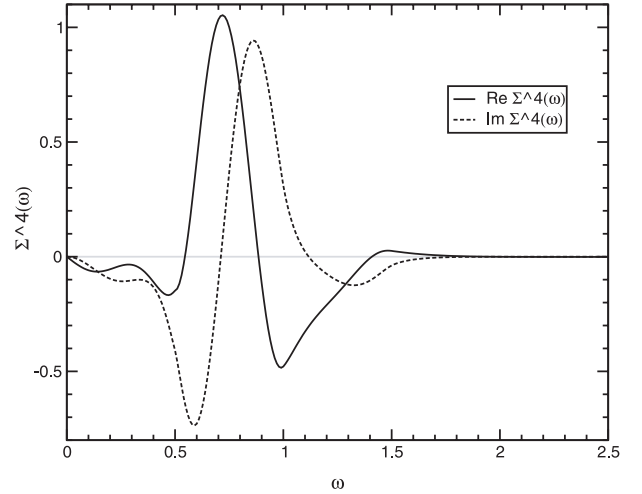Figure 7 shows the real and imaginary parts of the fourth-order self-energy, apart from the prefactor U^4.

The self-energy reproduces the Fermi-liquid relations (14) and (15) for small frequencies. Explicitly, we find from our numerical integrations

$$Z(U)^{-1} = 1 + 1.307[1] \left(\frac{U}{W}\right)^2 + 0.739[1] \left(\frac{U}{W}\right)^4 + \mathcal{O}(U^6) \tag{76}$$

and

$$\gamma(U) = 3.242[1] \left(\frac{U}{W}\right)^2 + 4.197[1] \left(\frac{U}{W}\right)^4 + \mathcal{O}(U^6), \tag{77}$$

where the number in brackets denotes the uncertainty in the last digit. The prefactor of the fourth-order term in $[Z(U)]^{-1}$ is smaller than reported in [6]. There, the momentum distribution was calculated using Rayleigh-Schrödinger stationary perturbation theory. We suspect that stationary perturbation theory is flawed when diagrams with self-energy insertions as in (71) occur.

Figure 7 shows that the fourth-order contribution to the self-energy becomes *positive* for $0.7W \leq \omega \leq 1.1W$. For small interaction strengths this positive contribution is compensated by the overall negative second-order self-energy. The sum of both terms is no longer negative for all frequencies above $U = 0.64W$, in contrast to the exact result (27). This limits the applicability of fourth-order perturbation theory to moderate interactions strengths.

3.3 Ground-state energy and average double occupancy

The ground-state energy can also be expanded in terms of powers in $(U/W)^2$,

$$\frac{E_0}{L} = -\frac{2W}{3\pi} + \alpha W \left(\frac{U}{W}\right)^2 + \beta W \left(\frac{U}{W}\right)^4 + \mathcal{O}(U^6). \tag{78}$$

We use this expansion in (24) and obtain

$$M_1 = \frac{2W}{3\pi} - 3\alpha W \left(\frac{U}{W}\right)^2 - 5\beta W \left(\frac{U}{W}\right)^4 + \mathcal{O}(U^6). \tag{79}$$

On the other hand, we may use (23) into which we insert the density of states from (21) which we can express in terms of the self-energy with the help of (17) and (18). For a better numerical accuracy, we calculate

$$a = \int_0^{3W/2} d\omega\, \omega \Im \left[-\Sigma_\sigma^{(2)}(\omega) - \sqrt{\left[\omega - \Sigma_\sigma^{(2)}(\omega)\right]^2 - 4} \right. $$
$$\left. + \sqrt{\omega^2 - 4} \right], \tag{80}$$

$$b = \int_0^{5W/2} d\omega\, \omega \Im \left[-\Sigma_\sigma^{(4)}(\omega) + \sqrt{\left[\omega - \Sigma_\sigma^{(2)}(\omega)\right]^2 - 4} \right. $$
$$\left. + \Sigma_\sigma^{(2)}(\omega) - \sqrt{\left[\omega - \Sigma_\sigma^{(2)}(\omega) - \Sigma_\sigma^{(4)}(\omega)\right]^2 - 4} \right]. \tag{81}$$

We fit the results to the form $a = a_0(U/W)^2 + a_1(U/W)^4$, and $b = b_0(U/W)^4 + b_1(U/W)^6$, and obtain for $\alpha = a_0/(3\pi)$ and $\beta = b_0/(5\pi)$

$$\alpha = -0.08346[1], \tag{82}$$

$$\beta = -0.0062[2]. \tag{83}$$

The prefactor of the fourth-order term, β, is an order of magnitude smaller than the second-order prefactor, α. This is very similar to the result for the single-impurity Anderson model addressed by Yamada and Yosida [24]. Therefore, we expect that the ground-state energy is reasonably well-described by fourth-order perturbation theory up to $U \leq W$.

Starting from

$$\overline{d}(U) = \frac{1}{4} + \frac{1}{L}\langle \hat{D}\rangle = \frac{1}{4} + \frac{1}{L}\frac{\partial E_0}{\partial U} \tag{84}$$

we obtain the fourth-order result

$$\overline{d}(U) = \frac{1}{4} + 2\alpha\left(\frac{U}{W}\right) + 4\beta\left(\frac{U}{W}\right)^3 + \mathcal{O}(U^5)$$
$$= 0.25 - 0.16692[2]\left(\frac{U}{W}\right) - 0.0248[8]\left(\frac{U}{W}\right)^3$$
$$+ \mathcal{O}(U^5) \tag{85}$$

for the average double occupancy at half band-filling. The average double occupancy is positive semi-definite. This criterion excludes the applicability of (85) for interaction strengths $U \geq 1.12[1]W$.

An even more stringent condition can be drawn from a comparison with the ground-state energy of the Mott-Hubbard insulator at half band-filling [14]. Up to third-order in $1/U$,

$$\frac{E_0}{L} = -\frac{U}{4} - \frac{W^2}{32U} - \frac{W^4}{512U^3} + \mathcal{O}(U^{-5}), \tag{86}$$

and

$$\overline{d}(U) = \frac{1}{32}\left(\frac{W}{U}\right)^2 + \frac{3}{512}\left(\frac{W}{U}\right)^4 + \mathcal{O}(U^{-6}). \tag{87}$$

If we use the $1/U$-expansion down to $U \geq W$, we find that the average double occupancy from the expansion in U and in $1/U$ become equal at the crossing point $U_{\text{cross}} = 1.056W$. Note that in [14] we estimated $U_{c,1} = 1.105[10]W$ for the opening of the gap. The fact that $U_{\text{cross}} \approx U_{c,1}$ might indicate that the Mott-Hubbard transition is indeed continuous at $U_{c,1} \equiv U_c$ without a discontinuity in the average double occupancy.

Within perturbation theory, the ground-state energies from weak and strong coupling do not become equal. Further terms in the $1/U$ expansion are also negative, so that equation (86) appears to give an upper bound to the ground-state energy. On the other hand, the perturbation expansion in U gives a maximum in $E_0(U)$ at $U = 1.12[1]W$ and thus provides a lower bound around $U = W$. Therefore, comparing energies from perturbation expansions will always result in a lower ground-state energy for the 'metal' (expansion in U) than for the 'insulator' (expansion in $1/U$). In the above case we find the minimum energy difference at U_{cross}, $\Delta E_0(U_{\text{cross}})/L = 0.018[1]W$.

Further observables will be discussed in Sections 4 and 5.

4 Dynamical mean-field theory (DMFT)

In this section, we summarize the Dynamical Mean-Field Theory and two of its numerical implementations. The self-consistent solution of the single-impurity Anderson model is carried out by the Fixed-Energy Exact Diagonalization (FE-ED) [14] and the Dynamical Density-Matrix Renormalization Group (DDMRG) [15,16]. We compare our results for the density of states from perturbation theory with those from FE-ED, DDMRG, the Numerical Renormalization Group (NRG) [10], and Iterated Perturbation Theory (IPT).

4.1 Single-impurity anderson model

In the limit of infinite dimensions [5] and under the conditions of translational invariance and convergence of perturbation theory in strong and weak coupling, lattice models for correlated electrons can be mapped onto single-impurity models [27,28,3], which must then be solved self-consistently. In general, these impurity models cannot be solved analytically.

For an approximate numerical treatment various different implementations are conceivable. One realization is the single-impurity Anderson model in the 'star geometry',

$$\hat{H}_{\text{SIAM}} = \sum_{\ell=1;\sigma}^{n_s-1} \epsilon_\ell \hat{\psi}_{\sigma;\ell}^+ \hat{\psi}_{\sigma;\ell} + U\left(\hat{d}_\uparrow^+\hat{d}_\uparrow - \frac{1}{2}\right)\left(\hat{d}_\downarrow^+\hat{d}_\downarrow - \frac{1}{2}\right)$$
$$+ \sum_\sigma \sum_{\ell=1}^{n_s-1} V_\ell\left(\hat{\psi}_{\sigma;\ell}^+\hat{d}_\sigma + \hat{d}_\sigma^+\hat{\psi}_{\sigma;\ell}\right), \tag{88}$$

where V_ℓ are real, positive hybridization matrix elements. The model describes the hybridization of an impurity site with an on-site Hubbard interaction to $n_s - 1$ bath sites without interaction at energies $\epsilon_1 < \epsilon_2 < \ldots < \epsilon_{n_s-1}$. In order to preserve particle-hole symmetry, we must choose $\epsilon_{n_s-\ell} = -\epsilon_\ell$, and $V_{n_s-\ell} = V_\ell$ for $\ell = 1, \ldots, n_s-1$. For even n_s, this implies that there is an energy level at $\epsilon_{n_s/2} = 0$, i.e., at the impurity level. For this bath site, which is absent for odd n_s, we expect particularly strong hybridization with the impurity level, so that large odd-even effects can be expected.

For a given set of parameters (ϵ_ℓ, V_ℓ) the model (88) defines a many-body problem for which the one-particle Green function

$$G_\sigma^{(n_s)}(t) = -\mathrm{i} \left\langle \hat{\mathcal{T}} \left[\hat{d}_\sigma(t) \hat{d}_\sigma^+ \right] \right\rangle_{\mathrm{SIAM}} \qquad (89)$$

must be calculated numerically. Here, $\langle \ldots \rangle_{\mathrm{SIAM}}$ implies the ground-state expectation value within the single-impurity Anderson model. The various implementations of the DMFT differ in the choice of this 'impurity solver' [29], denoted, e.g., as DMFT(FE-ED) or DMFT(DDMRG).

Ultimately, we will be interested in the limit $n_s \to \infty$ where the hybridization function

$$\mathcal{H}^{(n_s)}(\omega) = \sum_{\ell=1}^{n_s-1} \frac{V_\ell^2}{\omega - \epsilon_\ell + \mathrm{i}\eta\,\mathrm{sgn}(\omega)} \qquad (90)$$

is required to approach the hybridization function of the *continuous* problem smoothly,

$$\mathcal{H}(\omega) = \lim_{n_s \to \infty} \mathcal{H}^{(n_s)}(\omega). \qquad (91)$$

Correspondingly, the Green function is required to fulfill

$$G_\sigma(\omega) = \lim_{n_s \to \infty} G_\sigma^{(n_s)}(\omega). \qquad (92)$$

At self-consistency the Green function of the impurity problem describes the Hubbard model in infinite dimensions. As shown in [3], the hybridization function must obey the simple relation

$$\mathcal{H}(\omega) = G_\sigma(\omega) \qquad (93)$$

on the Bethe lattice. This equation closes the self-consistency cycle for the continuous problem: bath energies and hybridizations must be chosen in such a way that the one-particle Green function and the hybridization function fulfill (93).

4.2 Fixed-energy exact diagonalization (FE-ED)

In the FE-ED [14] for the metallic state, we choose to resolve the density of states within the frequency interval $|\omega| \leq W^*/2$. To this end, we partition the effective bandwidth W^* into equidistant intervals of width $\delta W = W^*/(n_s - 1)$,

$$I_\ell = [-W^*/2 + (\ell-1)\delta W, -W^*/2 + \ell\delta W], 1 \leq \ell \leq n_s-1. \qquad (94)$$

The energy levels are now fixed at the centers of I_ℓ,

$$\epsilon_\ell = -W^*/2 + (\ell - 1/2)\delta W, 1 \leq \ell \leq n_s - 1. \qquad (95)$$

For our calculations we choose $W^* = 9t = 2.25W$ which is sufficient to resolve the main features of the density of states (quasi-particle peak, Hubbard bands) for weak to intermediate coupling strengths, $U \leq W$. In the FE-ED, we can be sure that our resolution increases systematically as a function of $1/n_s$ which cannot be guaranteed in the Caffarel-Krauth implementation of the exact diagonalization [3,9,13,30].

For $n_s \leq 15$, we determine the impurity Green function using the (dynamical) Lanczos technique. The imaginary part of the Green function displays n_{L} peaks depending on the number $n_{\mathrm{L}} \approx 100$ states kept in the Lanczos diagonalization. We apply a constant broadening of width δW to the individual peaks in $\Im G_\sigma^{(n_s)}(\omega_r)$, $r = 1, \ldots, n_{\mathrm{L}}$. We then collect the weight into the intervals I_ℓ and assign this weight to $w_\ell = V_\ell^2$. Typically, the weight of the peaks at energies $|\omega_r| > W^*/2$ is very small. Thus we set

$$w_\ell = \int_{I_\ell} \mathrm{d}\omega \sum_{r=1}^{n_{\mathrm{L}}} \Im G_\sigma^{(n_s)}(\omega_r)$$
$$\times \frac{\Theta(\omega - \omega_r + \delta W/2) - \Theta(\omega - \omega_r - \delta W/2)}{\delta W}. \qquad (96)$$

In order to generate an educated input guess for $V_\ell = \sqrt{w_\ell}$, we use the results from fourth-order perturbation theory in (96). In the FE-ED, the self-consistency cycle is stable, i.e., different input choices result in the same self-consistent solution for a given n_s. This is not guaranteed in the Caffarel-Krauth exact-diagonalization scheme, as shown for the Mott-Hubbard insulator in [14]. The reason for the stability of the FE-ED is that the energies ϵ_ℓ are kept fixed. The n_s substantial peaks in $\Im G_\sigma^{(n_s)}(\omega_r)$ carry sufficient information to determine the n_s hybridization matrix elements V_ℓ. However, these n_s peaks are not sufficient to determine $2n_s$ parameters (ϵ_ℓ, V_ℓ) uniquely.

Figure 8 shows the converged hybridization function in FE-ED for $n_s = 14$ and $n_s = 15$ for $U = 0.4W = 1.6t$, in comparison with the results for the density of states from fourth-order perturbation theory. It is seen that the agreement is very good.

As seen in Figure 9, deviations are noticeable for $U = 0.6W = 2.4t$. Unfortunately, the resolution $\delta W = 9t/14 \approx 0.16W$ is still rather limited, and finite-size effects are appreciable around $\omega = 0.5W$. Therefore, it is unclear whether the differences in $D_\sigma(\omega)$ between FE-ED and perturbation theory around $\omega = 0.5W$ are due to finite-size effects of the FE-ED, or due to missing sixth-order terms in the perturbation expansion. The DDMRG which is able to treat much bigger systems allows us to resolve this issue.
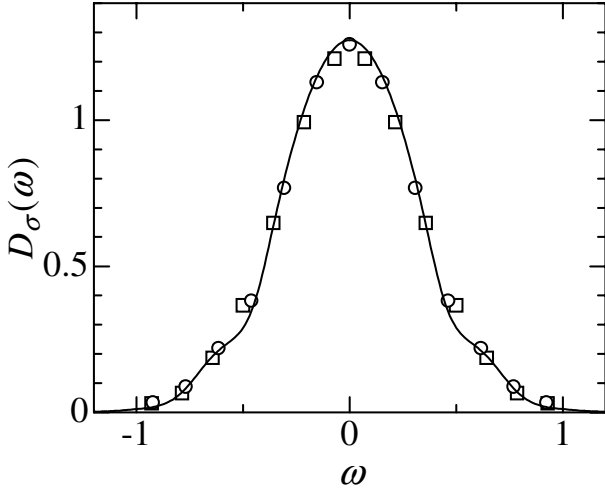
Fig. 8. Hybridization function $\mathcal{H}^{(n_s)}(\omega)$ for $n_s = 14$ (circles) and $n_s = 15$ (squares) in comparison with the density of states from fourth-order perturbation theory at $U = 0.4W$ (solid line); units $W = 4t \equiv 1$.
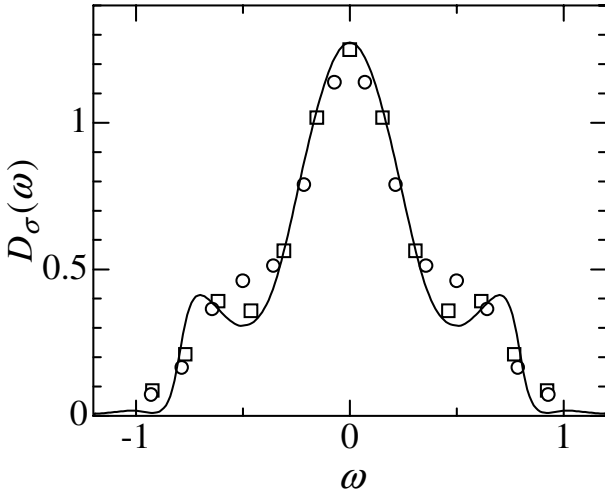

Fig. 9. Hybridization function $\mathcal{H}^{(n_s)}(\omega)$ for $n_s = 14$ (circles) and $n_s = 15$ (squares) in comparison with the density of states from fourth-order perturbation theory at $U = 0.6W$ (solid line); units $W = 4t \equiv 1$.

4.3 Dynamical density-matrix renormalization group (DDMRG)

The Density-Matrix Renormalization Group (DMRG) is a numerical method in which the energy functional

$$E(|\Psi\rangle) = \langle \Psi | \hat{H} | \Psi \rangle \qquad (97)$$

is minimized variationally in the subspace of normalized states $\langle \Psi | \Psi \rangle = 1$. This is done by carrying out a numerical diagonalization on a system of finite size and a renormalization on a part of this system. At each step of the renormalization, m density-matrix eigenstates of the subsystem are kept to build a variational basis of dimension $\mathcal{O}(m^2)$; for a review, see [31]. The optimal state for a given m, $|\Psi\rangle_{\mathrm{opt}}$, provides a variational bound for the ground-state

energy, $E_0^{\mathrm{var}} = {}_{\mathrm{opt}}\langle \Psi | \hat{H} | \Psi \rangle_{\mathrm{opt}}$. For one-dimensional lattice systems, this method provides a highly accurate estimate for ground-state properties of hundreds of interacting electrons. The accuracy of the energy, $E_0^{\mathrm{var}} = E_0 + \mathcal{O}(\varepsilon^2)$, is better than that of the variational ground state itself, $|\Psi\rangle_{\mathrm{opt}} = |\Psi_0\rangle + \mathcal{O}(\varepsilon)$. Typically, the error ε^2 scales as the weight P_m of the discarded density-matrix eigenstates.

In DDMRG [15], this concept is generalized to the minimization of a frequency-dependent functional. For the local Green function and $\omega \geq 0$, it reads

$$W_\eta(|\Psi\rangle; \omega) = \left\langle \Psi \middle| \left(E_0 + \omega - \hat{H} \right)^2 + \eta^2 \middle| \Psi \right\rangle$$
$$+ \eta \langle \Psi_0 | \hat{c}_{\boldsymbol{i},\sigma} | \Psi \rangle + \eta \left\langle \Psi \middle| \hat{c}_{\boldsymbol{i},\sigma}^+ \middle| \Psi_0 \right\rangle. \quad (98)$$

Here the frequency ω is fixed for an individual DDMRG run. The optimal state $|\Psi\rangle_{\mathrm{opt}}$ is the imaginary part of the so-called correction vector. The optimal functional becomes

$$W_\eta^{\mathrm{opt}}(\omega) = -\eta^2 \langle \Psi_0 | \hat{c}_{\boldsymbol{i},\sigma} \left[\left(E_0 + \omega - \hat{H} \right)^2 + \eta^2 \right]^{-1} \hat{c}_{\boldsymbol{i},\sigma}^+ | \Psi_0 \rangle$$
$$= -\eta^2 \sum_n \frac{|\langle \Psi_0 | \hat{c}_{\boldsymbol{i},\sigma} | \Psi_n \rangle|^2}{(E_0 + \omega - E_n)^2 + \eta^2}, \quad (99)$$

where $|\Psi_n\rangle$ and E_n are the exact eigenstates and energies of the Hamiltonian. The spectral representation (20) shows that, in the thermodynamic limit and up to a factor of $-\pi\eta$, the DDMRG provides the exact local density of states at frequency ω, convolved with a Lorentzian of width η,

$$D_\sigma^\eta(\omega) = -\frac{1}{\pi\eta} W_\eta^{\mathrm{opt}}(\omega). \quad (100)$$

The main advantage of this variational approach is that, as in the ground-state energy calculations, the optimal value of the functional (i.e., the density of states) is obtained with an accuracy of the order of ε^2 if the optimal state $|\Psi\rangle_{\mathrm{opt}}$ is calculated with an accuracy ε.

As the DMRG method is most accurate for systems with a quasi one-dimensional structure, we perform calculations of the single-impurity Anderson model (88) in its equivalent linear-chain form [32]

$$\hat{H}_{\mathrm{SIAM}} = U \left(\hat{d}_\uparrow^+ \hat{d}_\uparrow - \frac{1}{2} \right) \left(\hat{d}_\downarrow^+ \hat{d}_\downarrow - \frac{1}{2} \right)$$
$$+ V \sum_\sigma \left(\hat{f}_{\sigma;0}^+ \hat{d}_\sigma + \hat{d}_\sigma^+ \hat{f}_{\sigma;0} \right)$$
$$+ \sum_\sigma \sum_{\ell=0}^{n_s-2} \lambda_\ell \left(\hat{f}_{\sigma;\ell}^+ \hat{f}_{\sigma;\ell+1} + \hat{f}_{\sigma;\ell+1}^+ \hat{f}_{\sigma;\ell} \right). \quad (101)$$

The DDMRG provides the exact local density of states for a finite chain with n_s sites. To obtain the spectrum of an infinite chain, the broadening η must be scaled as a function of the system size [15]. If η is chosen too small, the DDMRG density of states displays finite-size peaks. If η is chosen too large, relevant information is smeared out. As an empirical fact, $\eta \approx W^*/n_s$ should be chosen, i.e., the

resolution scales as the inverse system size, as found for one-dimensional lattice models. The DDMRG technique for the single-impurity Anderson model will be described in more detail elsewhere [16].

In the DDMRG extension of the FE-ED, the limitations of the Lanczos technique are overcome in two ways. First, we may use bigger systems. The DDMRG can handle $n_s = 64$ sites on a workstation ($m = 300$ states kept in the renormalization) with CPU time as the limiting factor (48 hrs on a 500 MHz DEC-alpha workstation). In contrast, the exact diagonalization studies are seriously limited by memory constraints (3 GByte of memory for $n_s = 15$).

Second, the DDMRG provides the density of states at selected frequencies ω_i. Typically, we choose them to resolve the effective bandwidth W^* equidistantly, $\omega_{i+1} - \omega_i = \delta\omega \approx \eta \approx \delta W$. We then 'deconvolve' the DDMRG data by inverting the Lorentz transformation

$$D_\sigma^\eta(\omega_i) = \sum_j \frac{\delta\omega}{\pi} \frac{\eta}{\eta^2 + (\omega_i - \omega_j)^2} D_\sigma(\omega_j). \qquad (102)$$

The procedure can be repeated for different choices of the equidistant frequencies ω_i to get more values of $D_\sigma(\omega_j)$. In this way, the DDMRG provides a set of values $D_\sigma(\omega_j)$ for the density of states which, for the same n_s, is at least as dense as the set from the Lanczos diagonalization. In practice, we use from one to four different sets of frequencies, corresponding to a frequency resolution from η to $\eta/4$. Naturally, structures with an intrinsic width of less than η cannot be resolved with this procedure even if we use different sets of frequencies. The main advantage of this transformation, however, is that no extrapolation or scaling analysis of these values $D_\sigma(\omega_j)$ is necessary because they converge very quickly to the $n_s \to \infty$ limit. Therefore, with DDMRG we obtain a more accurate discrete representation of the density of states for a given n_s than within the Lanczos FE-ED.

An example for the non-interacting case is shown in Figure 10, where we have chosen $n_s = 64$, $W^* = 5t$, $\delta W = W^*/63$, and $\delta\omega = \eta = 0.1t$. This is a relevant test of accuracy because the non-interacting single-impurity Anderson model poses a non-trivial problem to DDMRG [16]. As seen in Figure 10, there is an excellent agreement between the 'deconvolved' numerical data for $n_s = 64$ and the exact result for $n_s \to \infty$.

The density of states from DDMRG and fourth-order perturbation theory also agree very nicely for $U = 0.4W$, as is seen in Figure 11. This result confirms the reliability of both the DDMRG and our perturbation theory at weak coupling.

The agreement is not perfect for $U = 0.6W$, as seen in Figure 12. The DDMRG is applicable at all interaction strengths, it is limited only by finite-size effects (resolution $\eta \propto 1/n_s$). Therefore, the deviations must be attributed to the sixth-order contributions which are missing in our perturbation expansion. The magnitude of the discrepancies around $\omega = 0.7W$ is indeed consistent with corrections of the order $0.6^2 = 36\%$ relative to the fourth-order term,
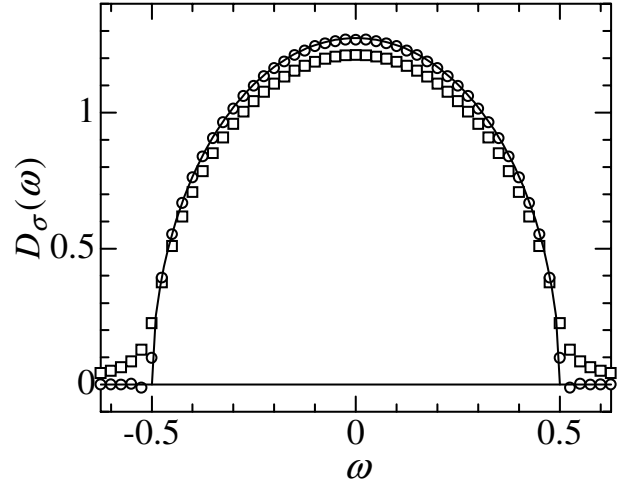

Fig. 10. Density of states for $U = 0$ from DDMRG on $n_s = 64$ sites, compared with the bare density of states $\rho_0(\omega)$ (6) (full line); units $W = 4t \equiv 1$. Squares: data from DDMRG for $\delta\omega = \eta = 0.1t$. Circles: DDMRG result after deconvolution.
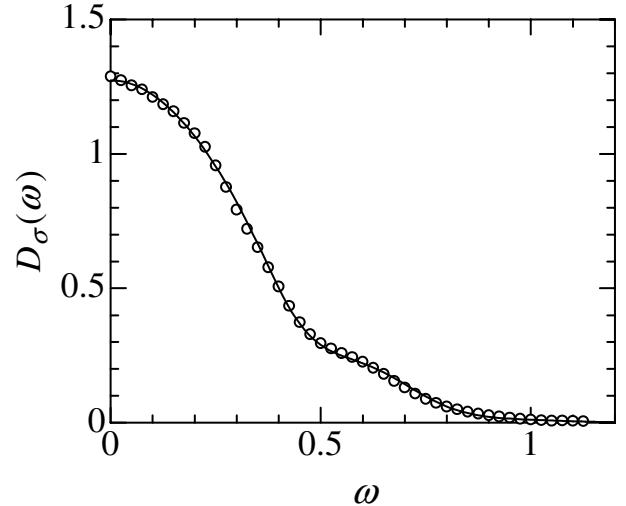

Fig. 11. Density of states for $U = 0.4W$ from DDMRG on $n_s = 32$ sites after deconvolution (circles), compared with fourth-order perturbation theory (full line); units $W = 4t \equiv 1$.

which dominates the second-order term around these frequencies. Therefore, we are confident that the DDMRG provides reliable results for all interaction strengths within its resolution limitations.

4.4 Numerical renormalization group (NRG)

The Numerical Renormalization Group (NRG) is a technique which aims to resolve accurately the self-energy and the density of states near $\omega = 0$. To this end, an exact diagonalization of the single-impurity model is performed at the nth step of the renormalization procedure for a frequency-interval I_ω^n around $\omega = 0$. The width of the frequency interval is cut in half at the next step of the renormalization procedure, starting at $I_\omega^0 = W^*$. Therefore, features near $\omega = 0$ are resolved with exponentially
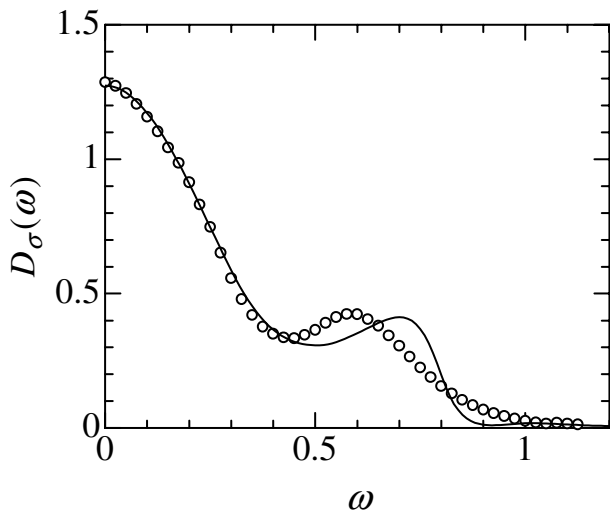
Fig. 12. Density of states for $U = 0.6W$ from DDMRG on $n_s = 32$ sites after deconvolution (circles), compared with fourth-order perturbation theory (full line); units $W = 4t \equiv 1$.

increasing accuracy whereas higher frequencies are represented by a few peaks which are broadened on a logarithmic scale [10]. As a result of this logarithmic mesh for the bath energies ϵ_ℓ, frequencies of the order of the Hubbard bands are resolved with a rather limited accuracy. Note that weight from the broadened Hubbard bands enters the low-energy physics again through the iterative self-consistency procedure.

Figure 13 shows the comparison of the self-energies from NRG and fourth-order perturbation theory for $U = 0.4W$. At intermediate to large frequencies, the NRG does not reproduce the fingerprints of the Hubbard bands as already seen in perturbation theory. The same quantitative differences are found for the real part of the self-energy.

As a consequence, the density of states in NRG does not show any signs of the Hubbard bands at $U = 0.4W$, in contrast to the exact result. Figure 14 shows the density of states from NRG as compared with perturbation theory for $U = 0.4W$ and $U = 0.6W$. Even at $U = 0.6W$, where the Hubbard bands are clearly visible, the NRG displays only a small shoulder. We conclude that the NRG has problems at frequencies of the order of the Hubbard bands whose height and positions cannot be determined reliably.

4.5 Iterated Perturbation Theory (IPT)

The IPT approximation to the self-energy of the $Z \to \infty$ Bethe lattice is given by [35,36]

$$\Sigma_\sigma^{\mathrm{IPT}}(\omega) = U^2 \int_{-\infty}^\infty \frac{\mathrm{d}\Omega}{2\pi\mathrm{i}} \Pi(\Omega)\mathcal{G}_\sigma(\omega - \Omega). \qquad (103)$$

Here, $\mathcal{G}_\sigma(\omega)$ is the host Green function

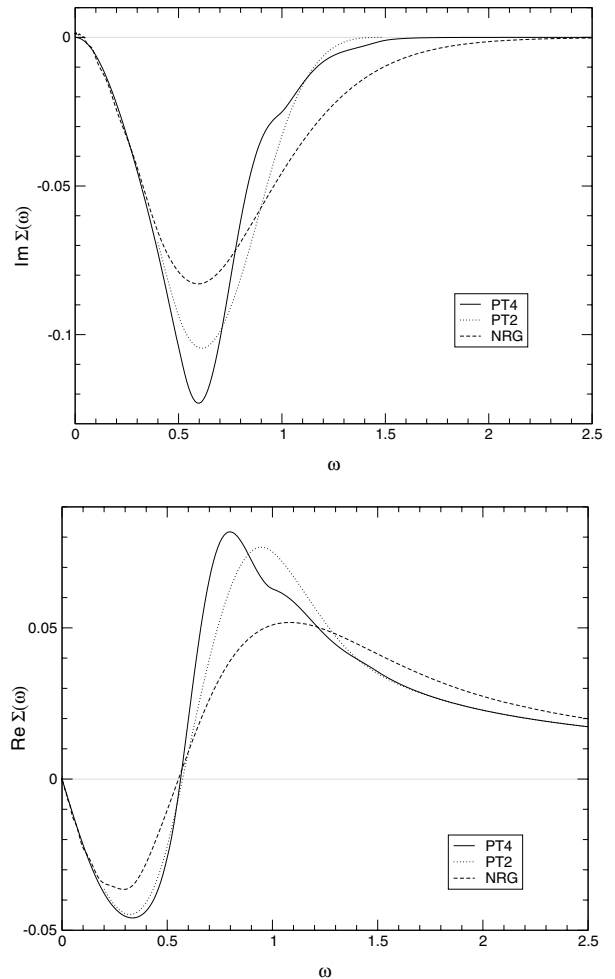$$\mathcal{G}_\sigma(\omega) = \frac{1}{\omega - G_\sigma(\omega)} \qquad (104)$$

Fig. 13. Real and imaginary parts of the self-energy from NRG for $U = 0.4W$ (dashed line), compared with fourth-order perturbation theory (full line) [33]. Also shown is the second-order self-energy (dotted line); units $W = 4t \equiv 1$.

and we have defined

$$\Pi(\omega) = -\int_{-\infty}^\infty \frac{\mathrm{d}\omega_1}{2\pi\mathrm{i}} \mathcal{G}_\sigma(\omega_1)\mathcal{G}_\sigma(\omega_1 - \omega) \qquad (105)$$

as the polarization bubble of the host Green functions.

By construction, IPT reduces to second-order perturbation theory in the limit of weak coupling. However, it omits the fourth-order diagrams with vertex corrections shown in Figures 3 and 4, whereas it weighs the other diagrams differently. Thus, it is uncontrolled at moderate interaction strengths.

Figure 14 shows the density of states from IPT for $U = 0.4W$ and $U = 0.6W$ in comparison with fourth-order perturbation theory. It is seen that the IPT does surprisingly well at weak coupling considering that it is exact only to $\mathcal{O}(U^2)$. In this limit and for half band-filling, it appears to be superior to the results from NRG. However, it does not reproduce the height of the Hubbard bands correctly.
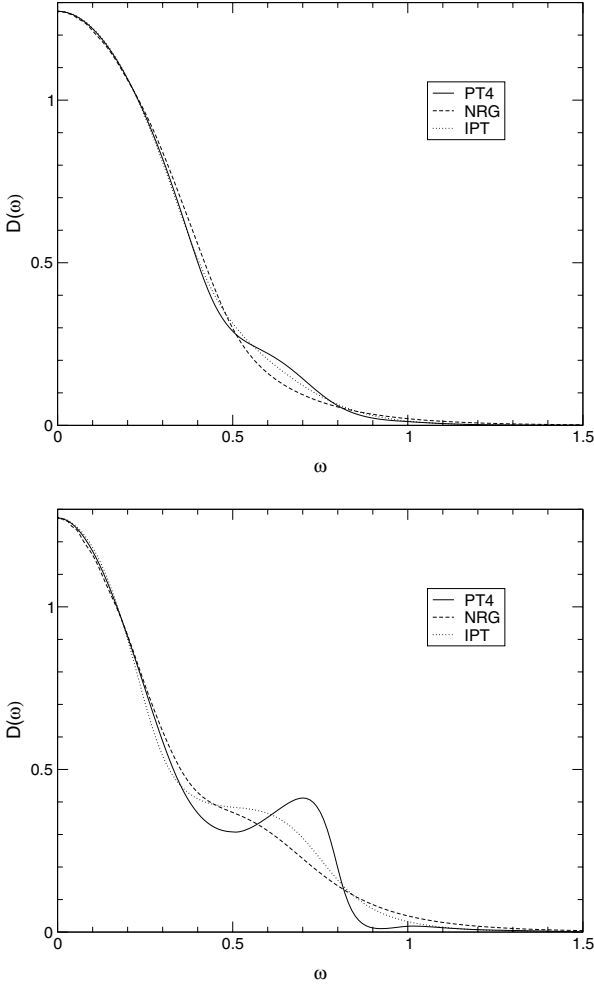
Fig. 14. Density of states for $U = 0.4W$ and $U = 0.6W$ from NRG (dashed lines) [33], IPT (dotted lines) [34], and fourth-order perturbation theory (full lines); units $W = 4t \equiv 1$.

5 Random dispersion approximation

In this section, we present numerical results from the Random Dispersion Approximation (RDA). It becomes exact for lattice electrons in high dimensions. In contrast to the FE-ED, DDMRG, or NRG, it is not based on the DMFT self-consistency equations. Moreover, the RDA does not require the convergence of the perturbation expansion. Therefore, it provides an independent check of the validity of perturbation theory and the DMFT approach.

5.1 Method

In the Random Dispersion Approximation, the dispersion relation $\epsilon(\boldsymbol{k})$ in the kinetic energy is replaced by a random quantity $\epsilon^{\mathrm{RDA}}(\boldsymbol{k})$ where the bare density of states acts as the probability distribution,

$$\rho(\epsilon) = \frac{1}{L} \sum_{\boldsymbol{k}} \delta(\epsilon - \epsilon^{\mathrm{RDA}}(\boldsymbol{k})), \qquad (106)$$

and all correlation functions factorize according to (5), etc. This is the characteristic property of the dispersion relation in infinite dimensions [2,6], so that the RDA with the semi-elliptic density of states (6) becomes exact for the Bethe lattice with infinite coordination number.

In order to put this idea into practice, we choose a one-dimensional lattice of L sites in momentum space

$$k_\ell = \frac{2\pi}{L} \left(-\frac{L+1}{2} + \ell \right), \quad (\ell = 1, \dots, L), \qquad (107)$$

and determine the dispersion relation $\epsilon(k)$ as the solution of the implicit equation

$$k/2 = (2\epsilon(k)/W) \left[1 - (2\epsilon(k)/W)^2 \right]^{1/2} + \arcsin\left(2\epsilon(k)/W \right). \qquad (108)$$

This choice guarantees $\rho(\epsilon) = \rho_0(\epsilon)$ in the thermodynamic limit.

Next, we choose a permutation $\mathcal{Q}_\sigma$ for each spin direction σ which permutes the sequence $\{1, \dots, L\}$ into $\{\mathcal{Q}_\sigma[1], \dots, \mathcal{Q}_\sigma[L]\}$. This defines a realization of the RDA dispersion, $\mathcal{Q} = [\mathcal{Q}_\uparrow, \mathcal{Q}_\downarrow]$. The numerical task is then the Lanczos diagonalization of the Hamiltonian

$$\hat{H}^{\mathcal{Q}} = \sum_\sigma \sum_{\ell=1}^{L} \epsilon(k_{\mathcal{Q}_\sigma[\ell]}) \hat{c}_{k_\ell, \sigma}^+ \hat{c}_{k_\ell, \sigma} + U\hat{D}. \qquad (109)$$

In this way we obtain the momentum distribution

$$n^{\mathcal{Q}}(\epsilon; U) = \frac{1}{2} \sum_\sigma \left. \langle \hat{n}_{k_\ell, \sigma} \rangle \right|_{\epsilon(k_\ell) = \epsilon}, \qquad (110)$$

where $\langle \dots \rangle$ denotes the ground-state expectation value for the realization $\mathcal{Q}$.

As a next step, we obtain all physical quantities for fixed system size L by averaging over $N_{\mathcal{Q}}$ realizations $\mathcal{Q}$. Typically, we choose at least $N_{\mathcal{Q}} = 100$ for $6 \le L \le 14$, and $N_{\mathcal{Q}} = 50$ for $L = 16$. For the physical quantities, we obtain Gaussian-shaped distributions for which we can determine the average values, e.g.,

$$n(\epsilon; U) = \frac{1}{N_{\mathcal{Q}}} \sum_{\mathcal{Q}} n^{\mathcal{Q}}(\epsilon; U) \qquad (111)$$

with accuracy $\mathcal{O}(1/N_{\mathcal{Q}})$.

In order to improve the quality of our distributions slightly, we impose a filter on our randomly chosen permutations. For a truly random dispersion, $L|t^{\mathrm{RDA}}(\ell)|^2 = \overline{\epsilon^2}$ is independent of ℓ [2]. Therefore, we discard those realizations for which

$$\sum_{\ell=1}^{L-1} \left[|t^{\mathcal{Q}_\sigma}(\ell)|^2 - \overline{\epsilon^2} \right]^2 > d_L \qquad (112)$$

with $d_L \approx 0.2$ for $L \le 16$. In this way, we admit about every second of the randomly chosen configurations. Note that there are of the order of $(L!)^2$ different realizations so that our filter does not introduce any unwanted bias.
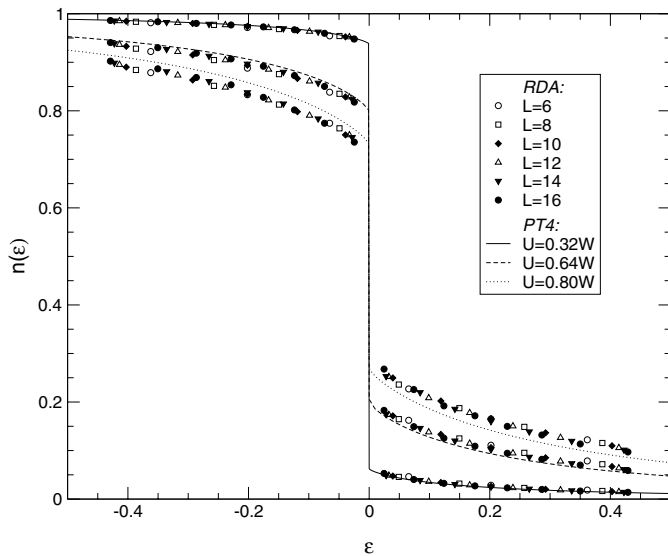
Fig. 15. Momentum distribution in RDA for $U = W/\pi \approx 0.32W$, $U = 2W/\pi \approx 0.64W$, and $U = 5W/(2\pi) \approx 0.80W$ for even system sizes $L \leq 16$. The lines are the result from fourth-order perturbation theory. Note the weak $\epsilon \ln \epsilon$ behavior near the discontinuity.
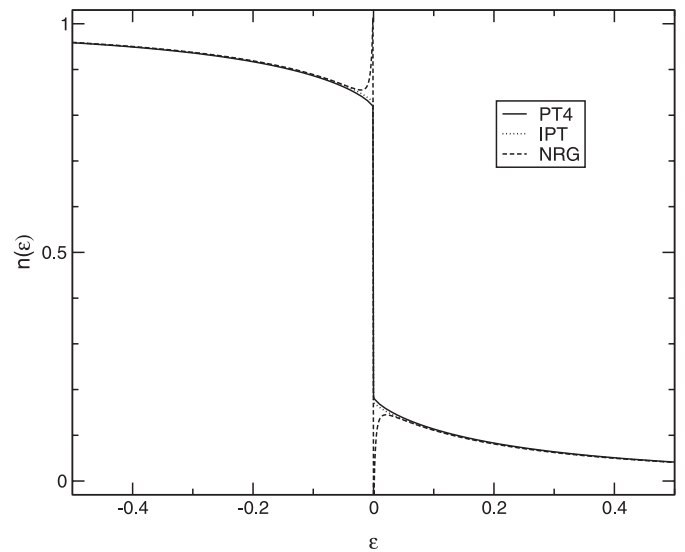

Fig. 16. Momentum distribution for $U = 0.6W$ in IPT (dotted line) [34], NRG (dashed line) [33], and fourth-order perturbation theory (full line). The deviations of NRG near the jump result from a small but finite positive imaginary part of the NRG self-energy around $\omega = 0$.

5.2 Momentum distribution

Figure 15 shows the RDA momentum distribution in comparison with results from perturbation theory. As seen from the figure, finite-size effects are rather small in the metallic phase. All values for the momentum distribution appear to fall onto almost the same curve. For small interaction strengths, the RDA data lie essentially on top of the perturbative results. Deviations for larger interactions can be attributed to missing higher-order corrections to our fourth-order result. Nevertheless, it is quite astonishing that fourth-order perturbation theory provides a sensible description of the momentum distribution for interaction strengths as large as $U \approx 0.8W$.

In Figure 16 we compare our results for the momentum distribution at $U = 0.6W$ from fourth-order perturbation theory with those from IPT and NRG. We see that both approaches describe the momentum distribution very well despite their shortcomings for the self-energy at intermediate frequencies. Apparently, for small to intermediate coupling strengths, the overall momentum distribution is not a very sensitive test for the quality of an approximation to the self-energy at intermediate frequencies.

A more sensitive quantity is the discontinuity of the momentum distribution at $\epsilon = 0$, see (30). Within the RDA, the quasi-particle weight for a given system size and U/W is obtained by fitting the momentum distribution $n(\epsilon; U)$ with a Fermi-liquid form (31) including the additional linear term. The resulting quasi-particle weight $Z(U; L)$ is displayed in Figure 17 for different U/W. These system-size dependent values are extrapolated to the thermodynamic limit by fitting to a second-order polynomial in $1/L$ for each U. Using a different form for the fit (such
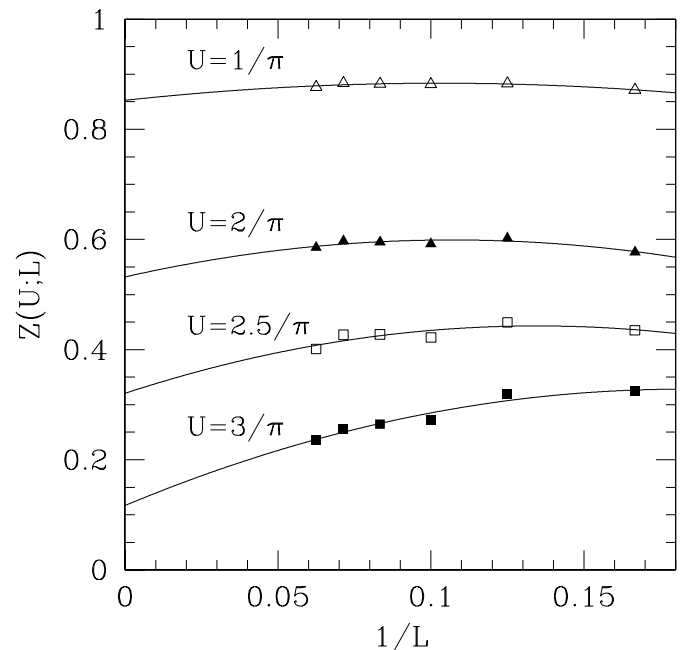

Fig. 17. Quasi-particle weight as a function of the inverse system size $1/L$ for $U/W = 0.32$, 0.64, 0.80, and 0.95 for the RDA. The solid lines indicate fits to second-order polynomials in $1/L$.

as a linear form) or excluding points for smaller system sizes lead to unsatisfactory results for small U. Note that the data and fitting methods of Figure 17 are the same as in Figure 4 of reference [6] except that the system size $L = 16$ has been added and additional configurations for $L = 14$ are included.
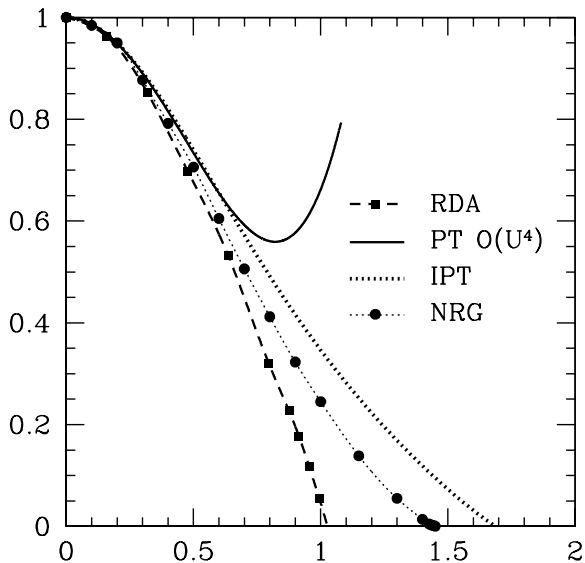
Fig. 18. Quasi-particle weight as a function of U/W in IPT (dotted line) [34], NRG (filled circles) [33], RDA (squares), and fourth-order perturbation theory (full line).

energy, the mean double occupancy, the momentum distribution, and the quasi-particle weight, and have compared it to various analytical and numerical approaches to the Hubbard model in infinite dimensions for the case of a Bethe lattice with infinite coordination number, i.e., a semi-circular bare density of states.

Our results show that, at half filling, it is not permitted to select only subclasses of diagrams because all diagrams contribute equally. The imaginary part of the self-energy to fourth order becomes positive at some frequency for $U = 0.64W$, which limits the applicability of our fourth-order results to moderate interaction strengths. For the momentum distribution and, in particular, the ground-state energy and the mean double occupancy, the perturbation expansion appears to be better behaved, i.e., the results remain sensible up to $U \approx W$. A similar observation had been made for the single-impurity Anderson model by Yamada and Yosida.

The Dynamical Mean-Field Theory (DMFT), which becomes exact in infinite dimensions, requires the self-consistent solution of a single-impurity Anderson model. Our results indicate that the Dynamical Density-Matrix Renormalization Group (DDMRG) is an excellent 'impurity solver'. Where Exact Diagonalization is hampered by finite-size effects ($n_s \leq 15$), the DDMRG treats much bigger systems, up to $n_s = 64$, and a new scheme for the deconvolution of the data further improves the frequency resolution. In this way, we obtain a very good agreement between the results from DDMRG and fourth-order perturbation theory where the latter is applicable.

The agreement is found to be less satisfactory with the results from Numerical Renormalization Group (NRG) at intermediate frequencies. The Hubbard bands which become discernible around $U = 0.4W$ are not resolved very well within the NRG scheme. It would be interesting to see whether a deconvolution of the NRG data could improve the agreement with fourth-order perturbation theory at the energy scale of the Hubbard bands. Iterated Perturbation Theory (IPT) works surprisingly well for $U \leq 0.6$ for all quantities tested. However, for larger interaction strengths, it seriously overestimates the quasi-particle weight and thus the stability of the metallic state.

The Random Dispersion Approximation (RDA), which also becomes exact in infinite dimensions, provides the momentum distribution and the quasi-particle weight. The results agree with those from fourth-order perturbation theory within the limits of its applicability. Unfortunately, for $U \leq W$, the momentum distribution and the quasi-particle weight turn out not be very sensitive quantities, i.e., all methods equally well reproduce the results from fourth-order perturbation theory. However, the RDA and NRG support two different scenarios for the Mott-Hubbard metal-insulator transition. The differences between NRG and RDA in the quasi-particle-weight become sizable only for $U > 0.8W$, a region which, unfortunately, cannot be accessed with fourth-order perturbation theory.

We hope that the DDMRG approach will enable us to investigate the region $U > 0.6W$ in more detail. Work in this direction is in progress.

In Figure 18 we show the quasi-particle weight as a function of U/W as obtained from IPT, NRG, RDA, and fourth-order perturbation theory. For fourth-order perturbation theory, we invert equation (76) which gives

$$ Z(U) = 1 - 1.307[1] \left(\frac{U}{W} \right)^2 + 0.969[2] \left(\frac{U}{W} \right)^4 + \mathcal{O}(U^6). $$
(113)

For the RDA, the extrapolated values from Figure 17 are plotted. In the region where fourth-order perturbation is reliable, $U \leq 0.6W$, the results agree with those from NRG and RDA within their numerical accuracy. Therefore, fourth-order perturbation theory cannot discriminate in favor of either of the two approaches which, however, support different scenarios for the Mott-Hubbard metal-insulator transition.

The quasi-particle weight from Iterated Perturbation Theory closely follows the fourth-order result to a point where (113) definitely overestimates $Z(U)$, e.g., for $U = 0.7W$. From this we conclude that IPT generally overestimates the stability of the metal.

6 Conclusions

In this work we have calculated the one-particle self-energy for the half-filled Hubbard model in the limit of infinite dimensions to fourth order in the interaction strength. We have reduced the four non-equivalent fourth-order diagrams to sets of two-dimensional integrals over real, tabulated functions over finite intervals. From the self-energy, we have derived the density of states, the ground-state

Appendix A: Momentum distribution near the discontinuity

Using the Luttinger relations (14) and (15) for a Fermi liquid, we evaluate (29) for $n_\sigma(\epsilon > 0) = (1 - Z(U))/2 + \delta n(\epsilon)$. Then,

$$\delta n_\sigma(\epsilon) = \int_{-\omega_c}^0 \frac{d\omega}{\pi} \frac{\gamma\omega^2}{(\omega/Z - \epsilon)^2 + \gamma^2\omega^4} + \dots, \quad (114)$$

apart from regular terms which come from the incoherent background in (25). Naturally, we are interested in the behavior close to the Fermi energy, i.e., for energies which fulfill

$$0 < Z(U)\epsilon < \omega_c. \quad (115)$$

Therefore, we require that

$$Z(U) \propto \omega_c \quad (116)$$

in order to observe a finite ϵ-interval in which the formulae below are applicable. Furthermore, we choose $\epsilon > 0$ so that we are above the jump in the distribution.

As can be seen by an explicit calculation, the dominant contribution for small ϵ comes from the frequencies $\omega = Z(U)\epsilon$. Then, we may ignore the term proportional to ω^4 in the denominator and we find

$$\delta n_\sigma(Z(U)\epsilon \ll \omega_c) = \frac{\gamma Z(U)^2\omega_c}{\pi} \int_{-1}^0 \frac{dx\, x^2}{(x - Z(U)\epsilon/\omega_c)^2}. \quad (117)$$

This approximation requires that

$$\epsilon \ll \frac{1}{Z(U)^2\gamma}. \quad (118)$$

This condition should correspond to (115) so that

$$\frac{1}{Z(U)\gamma} \propto \omega_c, \quad \text{i.e.,} \quad (119)$$

$$\gamma \propto (\omega_c)^{-2}. \quad (120)$$

The scaling laws (116) and (120) appear to be natural, given the Fermi liquid equations (14) and (15). To leading order in $\epsilon \ln \epsilon$, equation (117) results in (31).

If the above scaling laws (116) and (120) apply, there should be a finite region around $\epsilon = 0$ in which the $\epsilon \ln \epsilon$ dependence can be seen. However, its overall intensity scales down with an extra factor $Z(U)$.

Appendix B: Definition of help functions

Here we define the help functions which are necessary for the evaluations of the diagrams to fourth order. Explicit results are given for the semicircular density of states (6) in units of $W = 4t \equiv 1$.

We start with two functions which characterize the non-interacting Green function.

$$f(\omega) = \mathcal{P} \int_0^{W/2} d\epsilon \frac{\rho(\epsilon)}{\omega + \epsilon}, \quad (121)$$

$$\frac{\pi}{4} f\left(|\omega| \leq \frac{1}{2}\right) = \pi\omega - 1 - \sqrt{1 - 4\omega^2}\ln\left|\frac{2\omega}{1 + \sqrt{1 - 4\omega^2}}\right|, \quad (122)$$

$$\frac{\pi}{4} f\left(|\omega| > \frac{1}{2}\right) = \pi\omega - 1 - \text{sgn}(\omega)\sqrt{4\omega^2 - 1}\arccos\left(\frac{1}{2\omega}\right), \quad (123)$$

and

$$l(\omega) = f(\omega) - f(-\omega) = \Re G_\sigma^0(\omega) \quad (124)$$

$$= 8\omega\left(1 - \theta\left(|\omega| - 1/2\right)\sqrt{1 - \frac{1}{(4\omega^2)}}\right). \quad (125)$$

Next, we express the imaginary part of the bare polarization bubble in the form ($0 \leq a \leq W$)

$$h(a) = \int_0^{W/2} d\epsilon_1 \int_0^{W/2} d\epsilon_2\, \delta(a - \epsilon_1 - \epsilon_2)\rho(\epsilon_1)\rho(\epsilon_2) \quad (126)$$

$$= \theta(\frac{W}{2} - a) \int_0^a dy\rho\left(\frac{a + y}{2}\right)\rho\left(\frac{a - y}{2}\right)$$

$$+ \theta(a - \frac{W}{2}) \int_0^{W-a} dy\rho\left(\frac{a + y}{2}\right)\rho\left(\frac{a - y}{2}\right), \quad (127)$$

and

$$\Pi_\sigma^0(\omega) = -\int_0^W da\, h(a)\left(\frac{1}{\omega - a + i\eta} - \frac{1}{\omega + a - i\eta}\right). \quad (128)$$

Moreover, we need the Hilbert transform of $h(a)$

$$H(x) = \mathcal{P} \int_0^W da \frac{h(a)}{x + a}, \quad (129)$$

so that $\Im\Pi_\sigma^0(\omega \geq 0) = \pi h(\omega)$ and $\Re\Pi_\sigma^0(\omega) = H(\omega) + H(-\omega)$.

The imaginary part of the second-order self-energy requires the function

$$s(b) = \int_0^{W/2} d\epsilon_1 \int_0^{W/2} d\epsilon_2 \int_0^{W/2} d\epsilon_3$$

$$\times \rho(\epsilon_1)\rho(\epsilon_2)\rho(\epsilon_3)\delta(b - \epsilon_1 - \epsilon_2 - \epsilon_3), \quad (130)$$

which leads to

$$\Sigma_\sigma^{(2)}(\omega) = U^2 \int_0^{3W/2} \mathrm{d}b \, s(b) \left(\frac{1}{\omega + b - \mathrm{i}\eta} + \frac{1}{\omega - b + \mathrm{i}\eta} \right);$$

(131)

compare (41). Moreover, we need the Hilbert transform of $s(b)$

$$S(x) = \mathcal{P} \int_0^{3W/2} \mathrm{d}b \frac{s(b)}{x + b},$$

(132)

so that $\Im \Sigma_\sigma^{(2)}(\omega \geq 0) = -\pi U^2 s(\omega)$ and $\Re \Sigma_\sigma^{(2)}(\omega) = U^2[S(\omega) - S(-\omega)]$.

Finally, we introduce the derivative of the bare density of states as

$$\begin{aligned} d(x) &= \frac{\mathrm{d}\rho(x)}{\mathrm{d}x} \\ &= -\frac{16}{\pi} \frac{x}{\sqrt{1 - 4x^2}} \qquad \text{for} \quad |x| < 1/2. \end{aligned}$$

(133)

References

1. N.F. Mott, *Metal–Insulator Transitions*, 2nd edn. (Taylor and Francis, London, 1990)
2. F. Gebhard, *The Mott Metal–Insulator Transition* (Springer, Berlin, 1997)
3. A. Georges, G. Kotliar, W. Krauth, M.J. Rozenberg, Rev. Mod. Phys. **68**, 13 (1996)
4. M. Imada, A. Fujimori, Y. Tokura, Rev. Mod. Phys. **70**, 1039 (1998)
5. W. Metzner, D. Vollhardt, Phys. Rev. Lett. **62**, 324 (1989)
6. R.M. Noack, F. Gebhard, Phys. Rev. Lett. **82**, 1915 (1999)
7. J. Schlipf, M. Jarrell, P.G.J. van Dongen, N. Blümer, S. Kehren, T. Pruschke, D. Vollhardt, Phys. Rev. Lett. **82**, 4890 (1999)
8. M.J. Rozenberg, R. Chitra, G. Kotliar, Phys. Rev. Lett. **83**, 3498 (1999)
9. W. Krauth, Phys. Rev. B **62**, 6860 (2000)
10. R. Bulla, Phys. Rev. Lett. **83**, 136 (1999)
11. G. Kotliar, Eur. Phys. J. B **11**, 27 (1999)
12. R. Bulla, T.A. Costi, D. Vollhardt, Phys. Rev. B **64**, 045103 (2001)
13. R. Bulla, M. Potthoff, Eur. Phys. J. B **13**, 257 (2000); Y. Ōno, R. Bulla, A.C. Hewson, M. Potthoff, Eur. Phys. J. B **22**, 283 (2001)
14. M.P. Eastwood, F. Gebhard, E. Kalinowski, S. Nishimoto, R.M. Noack, Eur. Phys. J. B **35**, 155 (2003)
15. E. Jeckelmann, Phys. Rev. B **66**, 045114 (2002)
16. E. Jeckelmann, S. Nishimoto, to be published in J. Phys. Cond. Matt. (2004)
17. P.G.J. van Dongen, F. Gebhard, D. Vollhardt, Z. Phys. B **76**, 199 (1989)
18. E. Economou, *Green's Functions in Quantum Physics*, 2nd edn. (Springer, Berlin, 1983)
19. J. Hubbard, Proc. Roy. Soc. London Ser. A **276**, (1963) 238; Proc. Roy. Soc. London Ser. A **277**, 237 (1963)
20. A.L. Fetter, J.D. Walecka, *Quantum Theory of Many-Particle Systems* (McGraw–Hill, New York, 1971)
21. A.B. Migdal, Sov. Phys. JETP **5**, (1957) 333; J.M. Luttinger, J.C. Ward, Phys. Rev. **118**, 1417 (1960); J.M. Luttinger, Phys. Rev. **119**, 1153 (1960); Phys. Rev. **121**, 942 (1961)
22. E. Müller-Hartmann, Z. Phys. B **74**, 507 (1989); Z. Phys. B **76**, 211 (1989)
23. S. Schäfer, D.E. Logan, Phys. Rev. B **63**, 45122 (2001)
24. K. Yosida, K. Yamada, Prog. Theor. Phys. Suppl. **46**, 244 (1970); K. Yamada, Prog. Theor. Phys. **53**, 970 (1975)
25. J.K. Freericks, M. Jarrell, Phys. Rev. B **50**, 6939 (1994)
26. S. Mahlert, Ph.D. thesis (Marburg, 2003), unpublished
27. U. Brandt, C. Mielsch, Z. Phys. B **75**, 365 (1989); Z. Phys. B **79**, 295 (1990)
28. M. Jarrell, Phys. Rev. Lett. **69**, 168 (1992)
29. K. Held, I.A. Nekrasov, G. Keller, V. Eyert, N. Blümer, A.K. McMahan, R.T. Scalettar, T. Pruschke, V.I. Anisimov, D. Vollhardt in *Quantum Simulations of Complex Many-Body Systems: From Theory to Algorithms*, edited by J. Grotendorst, D. Marks, A. Muramatsu, NIC Series **10**, 175 (2002)
30. M. Caffarel, W. Krauth, Phys. Rev. Lett. **72**, 1545 (1994)
31. *Density–Matrix Renormalization*, edited by I. Peschel, X. Wang, M. Kaulke, K. Hallberg (Springer, Berlin, 1999)
32. See T. Costi in Ref. [31]
33. R. Bulla, private communication (2002)
34. M.P. Eastwood, private communication (2002)
35. M.J. Rozenberg, G. Kotliar, X.Y. Zhang, Phys. Rev. B **49**, 10181 (1994)
36. M.P. Eastwood, Ph.D. thesis (Oxford University, 1998), unpublished